Divergent changes in aerosol optical hygroscopicity and new particle formation during heatwaves of summer 2022

Yuhang Hao[1, a], Peizhao Li[1, a], Yafeng Gou[1], Zhenshuai Wang[1], Mi Tian[1], Yang Chen[2], Ye Kuang[3], Hanbing Xu[4], Fenglian Wan[1], Yuqian Luo[1], Wei Huang[5], Jing Chen[1, 6, *]

[1] College of Environment and Ecology, Chongqing University, Chongqing 400045, China

[2] Center for the Atmospheric Environment Research, Chongqing Institute of Green and Intelligent Technology, Chinese Academy of Sciences, Chongqing 400714, China

[3] Institute for Environmental and Climate Research, Jinan University, Guangzhou 511443, China

[4] Experimental Teaching Center, Sun Yat-sen University, Guangzhou 510275, China

[5] National Meteorological Center, China Meteorological Administration, Beijing 100081, China

[6] Key Laboratory of Three Gorges Reservoir Region's Eco-Environment, Ministry of Education, Chongqing University, Chongqing 400045, China

[a] These authors contributed equally

Correspondence to: Jing Chen (chen.jing@cqu.edu.cn)

Abstract. As a crucial climate-forcing driver, the aerosol optical enhancement factor (*f*(RH)) is significantly modulated by chemical compositions and the evolution of particle number size distribution (PNSD), e.g., during new particle formation (NPF). However, the mechanisms regulating aerosol optical hygroscopicity during different NPF days, particularly those influenced by heatwaves due to global warming, remain poorly understood. In the extremely hot summer of 2022 in urban Chongqing of southwest China, simultaneous measurements of aerosol optical and hygroscopic properties, PNSD, and bulk chemical compositions were conducted. Two distinct types of NPF were identified: the ones with relatively polluted period ($NPF_{polluted}$) and clean cases during heatwave-dominated period ($NPF_{clean,\ HW}$). Compared to the $NPF_{polluted}$ events, $NPF_{clean,\ HW}$ occurred approximately one hour earlier and the subsequent growth was prolonged, accompanied by a smaller aerosol effective radius (R_{eff}) and lower formation/growth rate during heatwaves. This agreed with the concurrently increased aerosol hemispheric backscattering fraction and scattering Ångström exponent. *f*(RH) was generally higher on NPF days in comparison to that for non-event cases in both periods. Moreover, heatwave-induced stronger photooxidation may intensify the formation of more hygroscopic secondary components, as well as the atmospheric aging/subsequent growth of both pre-existing and newly formed particles, thereby enhancing *f*(RH) especially during $NPF_{clean,\ HW}$ days. The promoted *f*(RH) and lowered R_{eff} could synergistically elevate the aerosol direct radiative forcing, specifically under persistent heatwave conditions. Further in-depth exploration on molecular-level characterizations and aerosol radiative impacts of both direct and indirect interactions during weather extremes (e.g., heatwaves) with the warming climate are recommended.

1 Introduction

Weather extremes (e.g., heatwaves) have become more and more frequent and intense largely due to the global climate change, and the heatwave-driven

environmental, climatic, and health effects have garnered widespread attention (Hauser et al., 2016; Sun et al., 2016). The China Climate Bulletin 2022 confirmed that the national average temperature reached an unprecedented high level since 2012 (China Meteorological Administration, 2022), and the risk of heatwaves in China will persist and potentially intensify in the future (Guo et al., 2016; Li et al., 2017). Extreme heatwave events could pose significant threats to human health, the survival of organisms, agriculture, and socio-economic activities (e.g., power supply restrictions) (Anderson and Bell, 2011; Ma et al., 2021; Su, 2021). Moreover, heatwaves can trigger natural disasters such as droughts and wildfires, affecting social stability (Sharma and Mujumdar, 2017).

Heatwaves could also affect the atmospheric physical and chemical processes by modulating ambient meteorological conditions. Specifically, extremely high temperature weather is typically characterized by a combination of intensified solar radiation with elevated temperature and low humidity levels. This could significantly affect the formation and evolution of secondary aerosols in the atmosphere (Bousiotis et al., 2021; Hamed et al., 2011; Kurtén et al., 2007), given that the air temperature is crucial for chemical reactions (Xu et al., 2011). New particle formation (NPF) serves as a crucial source of atmospheric particulate matter and plays a significant role in the secondary transformation processes in the atmosphere (Zhu et al., 2021). Generally, NPF involves the initial formation of thermodynamically stable clusters from condensable vapors (e.g., ammonia, sulfuric acid, and organic precursor gases) and subsequent growth of the formed clusters, eventually reaching detectable sizes or even larger dimensions (Kerminen et al., 2018; Kulmala et al., 2003, 2012). Over time, these newly formed particles have the potential to serve as cloud condensation nuclei (CCN), thereby impacting the global climate (Salma et al., 2016). NPF events normally introduce a sharp increase in the number concentration of nucleation mode particles within a short time, altering the particle number size distribution (PNSD). These variations in PNSD likely influence intrinsic physicochemical properties of aerosols, such as the optical hygroscopicity (Chen et al., 2014; Titos et al., 2016; Zhao et al., 2019).

Aerosol hygroscopicity plays a critical role in the atmospheric environment and climate change, given the complex interaction between aerosol particles and water vapor (Zhao et al., 2019; Zieger et al., 2011). Water uptake by aerosols not only alters the particle size and composition (e.g., as reflected in the aerosol refractive index) but also impacts aerosol scattering efficiency, which further contributes to the uncertainty in aerosol radiative forcing estimation (Titos et al., 2016, 2021). The aerosol optical hygroscopicity parameter, f(RH), defined as the ratio of the scattering coefficient at a certain RH to that of the dry condition, was widely used to describe the aerosol scattering enhancement through water uptake (Covert et al., 1972; Titos et al., 2016; Zhao et al., 2019). Numerous studies have demonstrated that f(RH) is influenced by the size distribution, in addition to particle chemical composition (Chen et al., 2014; Kuang et al., 2017; Petters and Kreidenweis, 2007; Quinn et al., 2005). There is currently limited research on the variations in aerosol optical hygroscopicity during NPF days despite significant changes in aerosol size distributions and chemical compositions, partly due to that newly formed particles insignificantly affect the optical properties of aerosols (Kuang et al., 2018). However, previous studies have observed the enhancement in aerosol hygroscopicity (Cheung et al., 2020; Wu et al., 2015, 2016) and extinction coefficients (Shen et al., 2011; Sun et al., 2024) during the subsequent growth of NPF. It is suggested that the influence of NPF on aerosol hygroscopicity was likely due to changes in aerosol chemical composition at different stages of NPF events (Cheung et al., 2020), whereas the subsequent particle growth associated with NPF events can significantly affect particle hygroscopicity as well (Wu et al., 2016). Although previous studies showed the dependences of aerosol hygroscopicity on chemical composition (Petters and Kreidenweis, 2007; Titos et al., 2016; Zhao et al., 2019) (e.g., the variation in composition of precursor species during NPF events), it is important to acknowledge that the utilized chemical compositions of NPF were either from $PM_{2.5}$ or PM_1 bulk data. This may differ from the corresponding composition of newly formed ultrafine particles primarily in the nucleation and Aitken modes, further introducing bias in exploring the impacts of NPF and subsequent growth on aerosol optical hygroscopicity. Hence, more

comprehensive investigations on the influencing mechanisms of aerosol optical hygroscopicity from different perspectives are required, e.g., for the aspects of the evolution of particle size distribution in modulating aerosol optical and hygroscopic properties (Tang et al., 2019; Zhao et al., 2019). Additionally, field observations on *f*(RH) under extreme weather conditions (e.g., heatwaves) are rather scarce, largely hindering our understanding of how weather extremes (e.g., extremely high temperature) influence the optical hygroscopic properties of aerosols. This knowledge gap further impedes comprehensive understanding of the aerosol water uptake property and resulted effects on air quality and the climate under varied synoptic conditions.

During the summer of 2022, a rare heatwave event raged throughout China, especially the Sichuan-Chongqing region of southwest China (Chen et al., 2024; Wang et al., 2024), with the daily maximum temperature exceeding 40 ℃ lasted for 29 days observed at Beibei meteorological station in Chongqing (Hao et al., 2023). This persistent heatwave not only impacted residents' daily lives significantly, but also affected the aerosol optical and hygroscopic properties likely through changed aerosol physicochemical characteristics and relevant atmospheric processing during the period. In this study, a field observation was conducted by using a combination of a home-built humidified nephelometer system and a scanning mobility particle sizer (SMPS), along with the total suspended particle (TSP) filter sampling. A main goal of this study is to investigate the influence of heatwaves on both aerosol optical hygroscopicity and the NPF with subsequent growth events, along with the related discrepancies. Furthermore, we aimed to explore the mechanisms behind the variability in *f*(RH) under different meteorological conditions and diverse NPF events. This study will further enrich insights into the potential environmental impacts due to variations in the aerosol optical hygroscopicity and size distribution, specifically under weather extremes (e.g., heatwaves) with the changing climate.

2 Data and Methods

2.1 Field observation

A continuous field observation on aerosol optical, hygroscopic and chemical properties was carried out from July 29 to August 19, 2022. The detailed description of the observation site is available in Supporting Information, S1. During the observation period, urban Chongqing suffered a rare heatwave (Fig. S1; Chen et al., 2024; Wang et al., 2024), which significantly affected the local transportation and industrial activities (Hao et al., 2023). China Meteorological Administration (CMA) defines heatwaves as three or more consecutive days with daily maximum temperature (T_{max}) above 35 °C (http://www.cmastd.cn/standardView.jspx?id=2103; Guo et al., 2016; Sun et al., 2014; Tan et al., 2007). Since no unified definition of heatwaves worldwide, the whole study period was categorized into two stages according to CMA's criteria of the daily T_{max} records and the Excess Heat Factor (EHF) metric proposed by Nairn and Fawcett (2014) (Fig. S2a): (1) the normally hot period from 29 July to 6 August (marked as P1); (2) the heatwave-dominated period from August 7-19 (marked as P2) characterized with the consistently occurrence of T_{max} exceeding 38 °C (approximately the last 25th percentile of temperature records for the whole observation period; Fig. S2b).

2.2 Instrumentation and methods

2.2.1 Measurements of aerosol optical hygroscopicity

The humidified nephelometer system, consisting of two three-wavelength (i.e., 450, 525, and 635 nm) nephelometers (Model Aurora 3000, Ecotech Inc.) and a humidification unit, was used to determine the aerosol light scattering enhancement factor, *f*(RH). Ambient air was firstly dried through a Nafion dryer (model MD-700, Perma Pure LLC) to ensure RH <35%, then split into two streams for both dry and humidified nephelometers operated in parallel. The flowrate for each nephelometer was 2.6 LPM. The aerosol scattering ($\sigma_{sca,\lambda}$) and backscattering coefficients ($\sigma_{bsca,\lambda}$) were detected in a dry state (RH <35%) and at a controlled RH level of 85 ± 1%,

166 respectively, with the humidification efficiency regulated automatically by a
167 temperature-controlled water bath. More details on the home-built humidified
168 nephelometer system are available in Kuang et al. (2017, 2020) and Xue et al. (2022).

169 Hence, *f*(RH) could be calculated as the ratio of the aerosol scattering coefficient
170 at a predefined RH ($\sigma_{sca,\ RH}$) to the dry ($\sigma_{sca,\ dry}$) state, i.e., *f*(RH) = $\sigma_{sca,\ RH}$ / $\sigma_{sca,\ dry}$
171 (Covert et al., 1972). In this study, the *f*(RH) discussed is mainly targeted for the 525
172 nm wavelength, unless otherwise specified. More information about the measurement
173 of humidified nephelometer system was illustrated in Sect. S2 of the supplement.

174 In additional to *f*(RH), aerosol optical parameters, such as scattering Ångström
175 exponent (SAE; Schuster et al., 2006) and hemispheric backscattering fraction (HBF;
176 Collaud Coen et al., 2007), were calculated as below:

177 $$SAE_{\lambda 1/\lambda 2} = \frac{-\ln\left(\sigma_{sca,\ \lambda 1}/\sigma_{sca,\ \lambda 2}\right)}{\ln\left(\lambda 1/\lambda 2\right)} \quad (1)$$

178 $$HBF_{\lambda} = \frac{\sigma_{bsca,\ \lambda}}{\sigma_{sca,\ \lambda}} \quad (2)$$

179 where $\sigma_{sca,\ \lambda}$ and $\sigma_{bsca,\ \lambda}$ represent the aerosol scattering and backscattering
180 coefficients at a specific wavelength λ (e.g., λ1, λ2), respectively.

181 Both HBF and SAE reflect crucial optical properties of aerosols, e.g., an elevated
182 HBF (or SAE) generally signifies a higher concentration (or a smaller particle size) of
183 fine particles within the aerosol population (Jefferson et al., 2017; Kuang et al., 2017;
184 Luoman et al., 2019). The HBF and SAE discussed in this study are targeted for the
185 dry condition, unless otherwise specified. Based on the measurements with the
186 humidified nephelometer system, the equivalent aerosol liquid water content (ALWC)
187 and the corresponding fraction of ALWC (f_W) can also be obtained (Kuang et al, 2018;
188 see Sect. S2 of the supplement).

189 The SMPS-measured concurrent particle number size distributions were further
190 utilized to calculate the aerosol effective radius (R_{eff}) and representative parameters
191 for NPF events, e.g., the formation rate (FR) and growth rate (GR) of new particle,
192 condensation sink (CS) and coagulation sink (CoagS) (Dal Maso et al., 2005; Kulmala
193 et al., 2012). More details are provided in the supplement (Sect. S5).

Results of the offline chemical analysis with TSP filter samples are provided in Sect. S3 and Fig. S3. It should be noted that certain secondary organics and crustal elements (e.g., Ca^{2+}, Mg^{2+}) that could exhibit a broader size distribution may contribute to the observed discrepancy in the total mass concentration between the 24-h TSP samples and daily mean $PM_{2.5}$ (of similar temporal variations; Fig.S3) (Duan et al., 2024; Kim et al., 2020; Xu et al., 2021). Nonetheless, previous studies reported that key components such as SNA (i.e., SO_4^{2-}, NO_3^-, and NH_4^+) and primary organics of $PM_{2.5}$ (or PM_{10}) were predominantly concentrated within the submicron size range (An et al., 2024; Bae et al., 2019; Chen et al., 2019; Duan et al., 2024; Kim et al., 2020; Xu et al., 2024). While the use of TSP samples contains some uncertainties, the bulk chemical information remains reasonable for characterizing the optical and hygroscopic properties of $PM_{2.5}$. The descriptions of simultaneous meteorological and air quality data can be found in Sect. S4, and the 48-h/72-h backward trajectory analysis was given in Sect. S5 of the supplement.

2.2.2 Determination of the aerosol direct radiative forcing (ADRF) enhancement factor

Given the high sensitivity of aerosol optical properties (e.g., f(RH)) to the changes in RH under real atmospheric conditions, the influence of RH, or rather the aerosol hygroscopicity, on ADRF can be quantitatively estimated with the radiative transfer model by the following equation (Chylek and Wong, 1995; Kotchenruther et al., 1999; L. Zhang et al., 2015):

$$\Delta F_R(RH) = -(S_0/4)\times[T_a^2\times(1-A_C)]\times[2\times(1-R_s)^2\times\beta(RH)\times\tau_s - 4\times R_s\times\tau_a] \quad (3)$$

where S_0 is the solar constant, T_a is the atmosphere transmittance, A_C is the fractional cloud amount, R_s is the albedo of the underlying surface, β(RH) is the upscattering fraction at a defined RH, τ_s and τ_a are the optical thicknesses of the aerosol layer due to light scattering and light absorption, respectively, which can be expressed as follows (Kotchenruther et al., 1999):

$$\tau_s = M\times\alpha_s\times f(RH), \tau_a = M\times\alpha_a \quad (4)$$

where M is the column burden of aerosol (unit: gm^{-2}), α_s is the mass scattering efficiency (MSE), and α_a is the mass absorption efficiency (MAE). The direct radiative forcing is usually calculated with the assumption that the absorption enhancement is negligible, in comparison to the aerosol scattering enhancement (Xia et al., 2023).

Hence, the dependence of ADRF on RH (i.e., $f_{RF}(RH)$) can be estimated by equation (5) (Chylek and Wong, 1995; Kotchenruther et al., 1999; L. Zhang et al., 2015):

$$f_{RF}(RH) = \frac{\Delta F_R(RH)}{\Delta F_R(dry)} = \frac{(1-R_s)^2 \times \beta(RH) \times \alpha_s \times f(RH) - 2 \times R_s \times \alpha_a}{(1-R_s)^2 \times \beta(dry) \times \alpha_s \times f(dry) - 2 \times R_s \times \alpha_a} \quad (5)$$

where the constant parameters used were $R_s = 0.15$, $\alpha_a = 0.3$ $m^2 \cdot g^{-1}$ (Hand and Malm, 2007; Fierz-Schmidhauser et al., 2010). It should be noted that the assumed constant α_a might introduce some uncertainty in the calculated $f_{RF}(RH)$, given the fact that the contribution of absorption by brown carbon was unknown, although the mass fraction of BC in TSP remained almost constant (i.e., 4.6% ± 1.1%, Fig. S3) during the observation period. The parameter α_s was calculated by dividing $\sigma_{sca,\,525}$ in the dry condition by the mass concentration of $PM_{2.5}$ (i.e., $\alpha_s = \sigma_{sca,\,525} / PM_{2.5}$). β could be calculated empirically from the measured HBF: $\beta = 0.0817 + 1.8495 \times HBF - 2.9682 \times HBF^2$ (Delene and Ogren, 2002).

3 Results and discussion

3.1 Overview of the aerosol optical hygroscopicity and PNSD measurements

Figure 1 displayed the time series of the measured aerosol scattering coefficients, *f*(RH), PNSD, and the corresponding meteorological conditions and air pollutants during the study period. A sharp decrease in aerosol scattering coefficients and $PM_{2.5}$, accompanied with the continuous excellent visibility over 20 km was observed after August 6, indicating a markedly cleaner environment during P2 in comparison to P1 in summer 2022 of Chongqing. This could be largely attributed to the reduction in anthropogenic emissions (e.g., NO_2, CO, except SO_2) from limited outdoor activities

influenced by the heatwaves in P2, as well as partly suspended industries and transportation to alleviate the power shortage issue (Chen et al., 2024). Notably, the increased wind speed and enhanced mixing layer height (MLH) also enabled a more favorable atmospheric diffusion condition in P2, facilitating the dilution of surface air pollutants (Zhang et al., 2008). However, a higher mass concentration of SO_2 was observed in the P2 period, likely due to a surge in electricity demand and resulted higher emissions from power plants operating almost at full capacity during the heatwave (Su, 2021; Teng et al., 2022). Moreover, significant discrepancies in the aerosol optical and hygroscopic properties were observed under different synoptic conditions (Table S2). Both HBF and SAE were higher during the P2 period, aligning with the smaller R_{eff} (Table S2). The f(RH) was found to be relatively higher (p <0.05) in heatwave days, with the mean values of 1.61 ± 0.12 and 1.71 ± 0.15 during the P1 and P2 periods, respectively. Differently, ALWC was more abundant during the normally hot P1 period than the heatwave-dominated P2 period. This is likely due to that the derivation algorithm of ALWC utilized in this study (Kuang et al., 2018) was partly dependent on (e.g., positively correlated) the dry aerosol scattering coefficient, or rather the aerosol volume concentration in the dry condition (refer to Sect. S3 and Fig. S11 of the supplement). The mean $\sigma_{sca,\,525}$ for P2 was about 46.8% of that for the P1 period, and the corresponding mean level of ALWC was approximately 55.8% of that for P1. This partly agrees with the stronger aerosol optical hygroscopicity with a marginally higher f_W during the P2 period, highlighting a complex interaction between the optical enhancement and aerosol physicochemical properties.

The particle number size distribution data suggested that NPF events appeared in about half the number of observation days (Fig. 1i), with an overall occurrence frequency of 52.4% (Fig. S4a). This suggests the rather frequent summer NPF events in Chongqing, notably higher than those observed in other regions of the world, e.g., Beijing (16.7%, Deng et al., 2020; ~20%, Wang et al., 2013), Dongguan (4%, Tao et al., 2023), Hyytiälä (<40%, Dada et al., 2017) and LiLLE (<20%, Crumeyrolle et al., 2023). Moreover, the frequent NPF events during heatwaves formed substantially ultrafine particles that are of less contribution to aerosol optical properties in

comparison to large particles (Fig. S13), partially explaining the significantly lower levels of total scattering coefficients observed during the P2 period. It should be noted that the hourly $\sigma_{sca,\,525}$ values during the P2 period were exclusively below 100 Mm^{-1} (approximately the last 10th percentile of $\sigma_{sca,\,525}$ data, regarded as the threshold value of relatively polluted cases; Fig. S2c), suggesting a much cleaner environment compared to the relatively polluted P1 period. Correspondingly, NPF events occurring during the relatively polluted P1 period (as detailed in section 3.2) were defined as $NPF_{polluted}$, while cases during the cleaner and heatwave-dominated P2 period were classified as $NPF_{clean,\,HW}$.

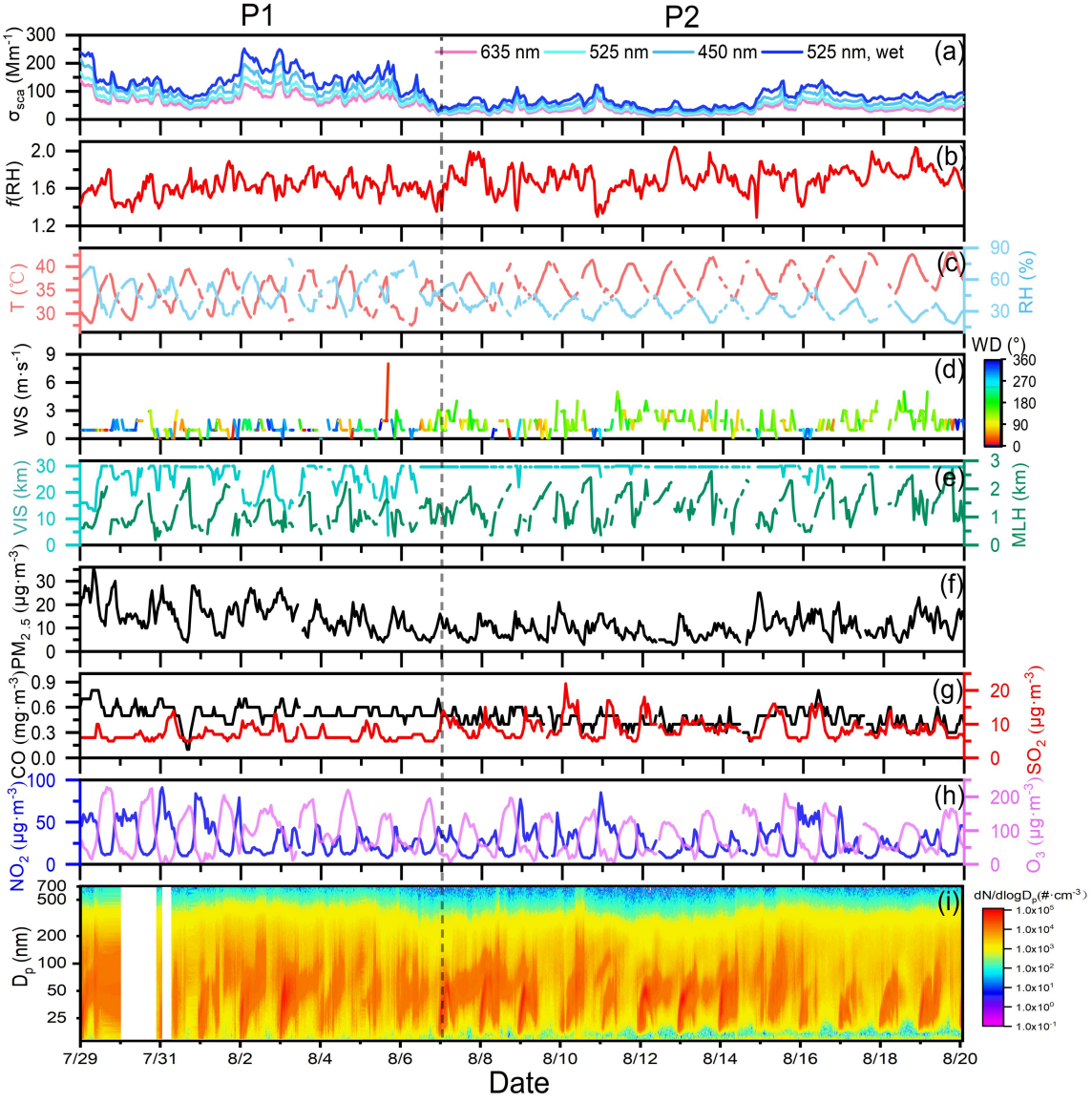

Figure 1. Time series of the measured aerosol scattering coefficients, *f*(RH), meteorological conditions, air pollutants, and particle number size distribution during the study period.

3.2 Characteristics of NPF events in different periods

Aside from gaseous precursors (e.g., SO_2, volatile organic compounds), meteorological conditions also play a key role in the occurrence of NPF events. In brief, NPF events are more likely to appear under sunny and clean conditions (Bousiotis et al., 2021; Crumeyrolle et al., 2023; Deng et al., 2021; Wang et al., 2017). The backward trajectory analysis revealed that the southerly breeze was predominant during the study period (Fig. S4b). Although the surface wind vector slightly varied between the P1 and P2 periods, this consistency in air mass origins suggests that some other factors (e.g., changes in environmental conditions and emissions of gaseous precursors under heatwaves) could have played a crucial role in modulating NPF events. To further explore the characteristics of NPF events in different periods, the time-averaged diurnal variations of meteorological parameters and air pollutant concentrations during both NPF events and non-event days are presented in Fig. 2.

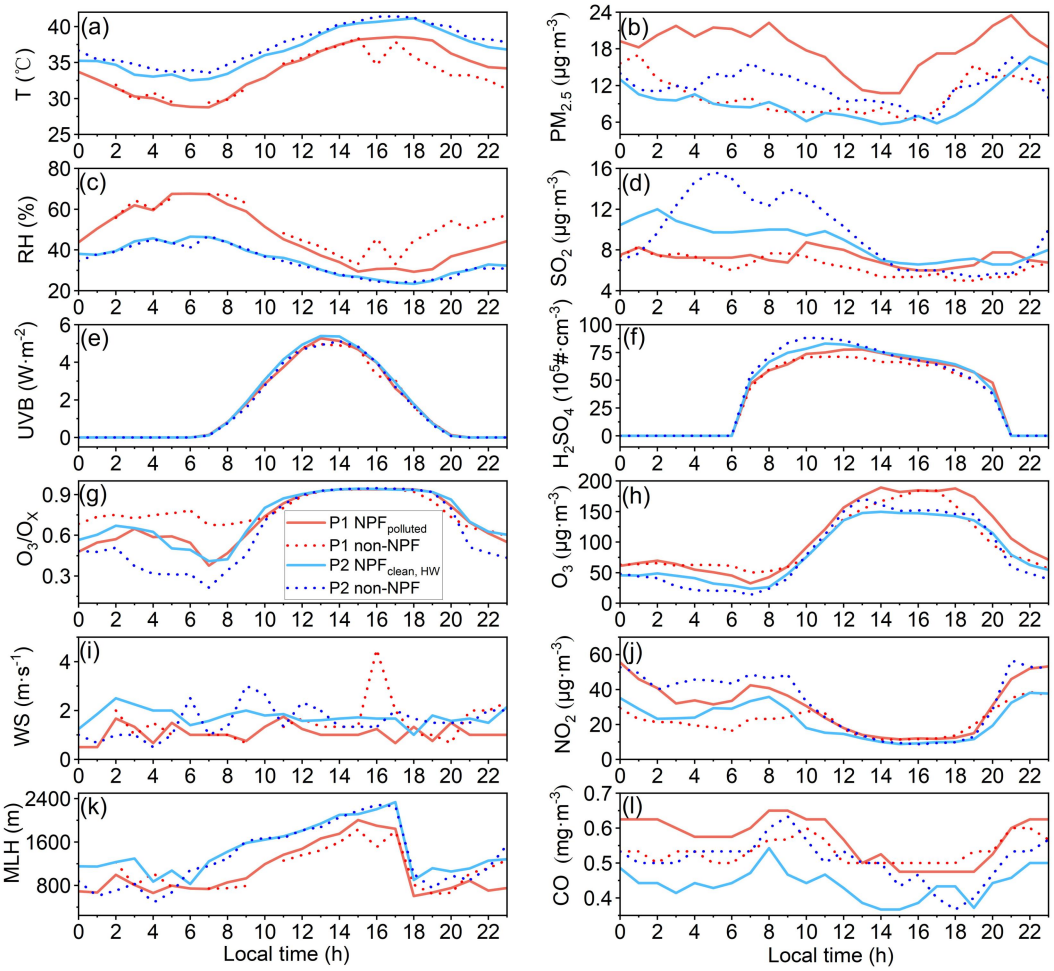

Figure 2. Diurnal variations of temperature **(a)**, $PM_{2.5}$ mass loading **(b)**, RH **(c)**, SO_2 **(d)**, UVB **(e)**, H_2SO_4 **(f)**, O_3/O_X **(g)**, O_3 **(h)**, WS **(i)**, NO_2 **(j)**, MLH **(k)** and CO **(l)** during P1 (red) and P2 (blue) NPF days (solid line), as well as the corresponding non-event days (dash line).

As stated in Sect.3.1, NPF events during the P1 period tended to occur in relatively polluted environments compared to that of P2 $NPF_{clean,\ HW}$ events, as evidenced by the frequent occurrence of $\sigma_{sca,\ 525}$ >100 Mm^{-1}, increased air pollutant concentrations and lower visibility levels during P1 (Table S2, Fig. 1). Additionally, the mean CS of the $NPF_{polluted}$ events was above 0.015 s^{-1} (Table S2), which could be considered as the "polluted" NPF cases (Shang et al., 2023). On P2 $NPF_{clean,\ HW}$ days, the overall mean $\sigma_{sca,\ 525}$ was 33.2 ± 11.7 Mm^{-1}, decreased by 68.0% (39.3%) in comparison to that for P1 $NPF_{polluted}$ days (P2 non-event days). In addition, the mean $PM_{2.5}$ concentration was even lower than 10.0 $\mu g \cdot m^{-3}$, and the corresponding visibility

level was almost maintained at 30 km (Fig. 1e). All the above implies that the P2 $NPF_{clean,\ HW}$ events were generally accompanied with a much cleaner environment. It is notable that the increase in SO_2 concentration after 9:00 LT (Fig. 2d), along with the significant decrease in $PM_{2.5}$ mass loadings after 8:00 LT during P1 $NPF_{polluted}$ events (Fig. 2b), likely favored the occurrence of NPF events. The higher gas-phase sulfuric acid (i.e., H_2SO_4, as estimated with the UVB and SO_2 concentration, Lu et al., 2019, Sect. S4) on the same NPF days (Fig. 2f), further suggesting that sulfuric acid concentration was a critical factor for the occurrence of P1 $NPF_{polluted}$ events.

The diurnal evolutions of meteorological conditions (e.g., T, RH, MLH) for NPF events were distinct between P1 and P2 periods, although relatively insignificant differences were observed for both NPF days and non-event days within a same period (Fig. 2). This likely suggests that meteorological factors might not be the predominant determining factor of NPF occurrence during the heatwaves of 2022 summer in urban Chongqing, while NPF could be accompanied with quite different meteorological conditions depending on gaseous precursors and preexisting condensation sinks. For instance, the $NPF_{clean,\ HW}$ events were typically of clean-type NPF, characterized with lower background aerosol loading, higher temperature and favorable atmospheric dispersion capacity with the higher MLH. However, it is reported that excessive heat can increase the evaporation rate of critical acid-base clusters during the nucleation process and reduce the stability of initial molecular clusters (Bousiotis et al., 2021; Kurtén et al., 2007; Zhang et al., 2012), in line with a recent study that NPF events were weaker during heatwaves in Siberian boreal forest due to the unstable clusters (Garmash et al., 2024). On the other hand, the emission rate of biogenic VOCs ($BVOC_S$, e.g., isoprene, monoterpene) from nearby plants and trees would decrease when temperature exceeded around 40 °C (Guenther et al., 1993; Pierce and Waldruff, 1991), despite that BVOCs plays a key role in the nucleation mechanism of NPF (Wang et al., 2017; Zhang et al., 2004). Hence, the even higher temperature (e.g., T >40 ℃) likely suppressed the nucleation processes and the subsequent growth of nucleation mode particles on P2 non-event days (Fig. S6b2), in spite of higher concentrations of SO_2 and H_2SO_4.

To further investigate the effect of heatwave on NPF events, the diurnal variations of PNSD, R_{eff} and particle mode diameter (D_{mode}) were shown in Fig. S6. Aerosol number and volume concentrations, as well as R_{eff}, for different modes were illustrated in Figs. S7-8, and the relationship between temperature and the duration of NPF events was displayed in Fig. S9. Distinct particle size distributions were observed for different NPF event days. While the number concentrations of Aitken mode particles ($N_{Ait.}$) were comparable during NPF days of both periods, the corresponding number concentration of nucleation mode ($N_{Nuc.}$) was significantly higher on P1 $NPF_{polluted}$ days (1880.8 ± 2261.5 cm^{-3}) than that for P2 NPF cases (1132.0 ± 1333.5 cm^{-3}) (Fig. 1i, Fig. S7). The reduced $N_{Nuc.}$ during P2 period was likely attributed to the influence of transport on the local nucleation process (Fig. S4; Cai et al., 2023; Lee et al., 2019). Namely, some nucleation mode particles transported from upwind regions had undergone atmospheric aging thereby a certain degree of growth upon arrival (Cai et al., 2023), resulting in relatively lower concentrations of smaller-sized particles than the case of locally formed. However, the NPF events under heatwaves usually initiated earlier (Fig. S9), with the $N_{Nuc.}$ in P2 $NPF_{clean, HW}$ cases peaked about an hour earlier in comparison to $NPF_{polluted}$ days (Fig. S8a). The D_{mode} on P2 $NPF_{clean, HW}$ days also reached its minimum earlier than that on P1 $NPF_{polluted}$ days (Fig. S6). Since the sunrise and sunset time did not significantly vary within the study period (i.e., less than a half hour discrepancy), heatwaves likely provided more favorable conditions (e.g., enhanced volatile gaseous emissions, low RH; Bousiotis et al., 2021; Hamed et al., 2007; Wang et al., 2024) for the occurrence of NPF events in urban Chongqing. This is supported by the earlier start time of $NPF_{clean, HW}$ corresponding to higher temperature ranges (Fig. S9). Furthermore, the end time of subsequent particle growth during P2 period was even later (i.e., ~ 21:00 LT) than that of P1 cases (Fig. S9). Given that the growth rates of new particles were generally lower during P2 $NPF_{clean, HW}$ events (Table S2), these explosively formed new particles could persist longer in the warmer atmosphere and probably undergo aging processes with a relatively higher oxidation degree. This is supported by the commonly higher ratios of secondary organic carbon (SOC) to organic carbon (OC)

(i.e., SOC/OC >0.5) during the $NPF_{clean, HW}$ days (Fig. S3b). In addition, aerosol R_{eff} was significantly smaller on the $NPF_{clean, HW}$ days under heatwave conditions. The R_{eff} and D_{mode} nearly kept at a same level below/approaching 50 nm during the subsequent growth on the P2 $NPF_{clean, HW}$ days, while the R_{eff} was generally above 50 nm and larger than D_{mode} for both P1 $NPF_{polluted}$ cases and non-event days (Fig. S6). The diurnal patterns of aerosol volume concentrations for different size modes were similar to that of aerosol number concentrations during NPF events (Fig. S8b1-b3). However, both the R_{eff} of Aitken mode particles ($R_{Ait.}$) and accumulation mode particles ($R_{Acc.}$) were smaller during P2 $NPF_{clean, HW}$ events than that of P1 $NPF_{polluted}$ events (Fig. S8c2-c3), which may further influence size-dependent aerosol optical and hygroscopic properties (e.g., $\sigma_{sca, 525}$, HBF, SAE, f(RH)). The decrease in $R_{Ait.}$ and $R_{Acc.}$ during heatwaves could be attributed to three factors: (1) evaporation of the outer layer of particles and unstable clusters due to heatwaves (Bousiotis et al., 2021; Cusack et al., 2013; Deng et al., 2020; Garmash et al., 2024; Li et al., 2019); (2) lower FR and GR of particles under the cleaner environment (Table S2); (3) reduced emissions of larger primary particles during the P2 period.

3.3 Characteristics of the aerosol optical and hygroscopic properties on different types of NPF days

Diurnal variations of the aerosol optical and hygroscopic parameters during different NPF days were shown in Fig. 3, and the corresponding results for non-event days can refer to Fig. S10. Generally, $\sigma_{sca, 525}$ possessed a similar bimodal diurnal pattern to that of the accumulation mode aerosol volume concentration ($V_{Acc.}$) (Fig. S8b3), as supported by the positive correlation between $\sigma_{sca, 525}$ and SMPS-measured aerosol volume concentration (Fig. S12). This is also consistent with the Mie theory, with a stronger increase in the scattering efficiency for accumulation mode particles (Titos et al., 2021). The diurnal pattern of $\sigma_{sca, 525}$ also varied distinctly between different NPF days. Specifically, a minor peak of $\sigma_{sca, 525}$ around 12:00 LT (Fig. 3a) was influenced by the newly formed particles during P2 $NPF_{clean, HW}$ events, which contributed more significantly to the aerosol number and volume concentrations

within 100 nm size ranges in markedly clean environments (Fig. S5c1, c2). Instead of a noontime peak, $\sigma_{sca,\ 525}$ was observed with an early peak around the morning rush hours and a maximum value similarly occurred at the nighttime on P1 $NPF_{polluted}$ days.

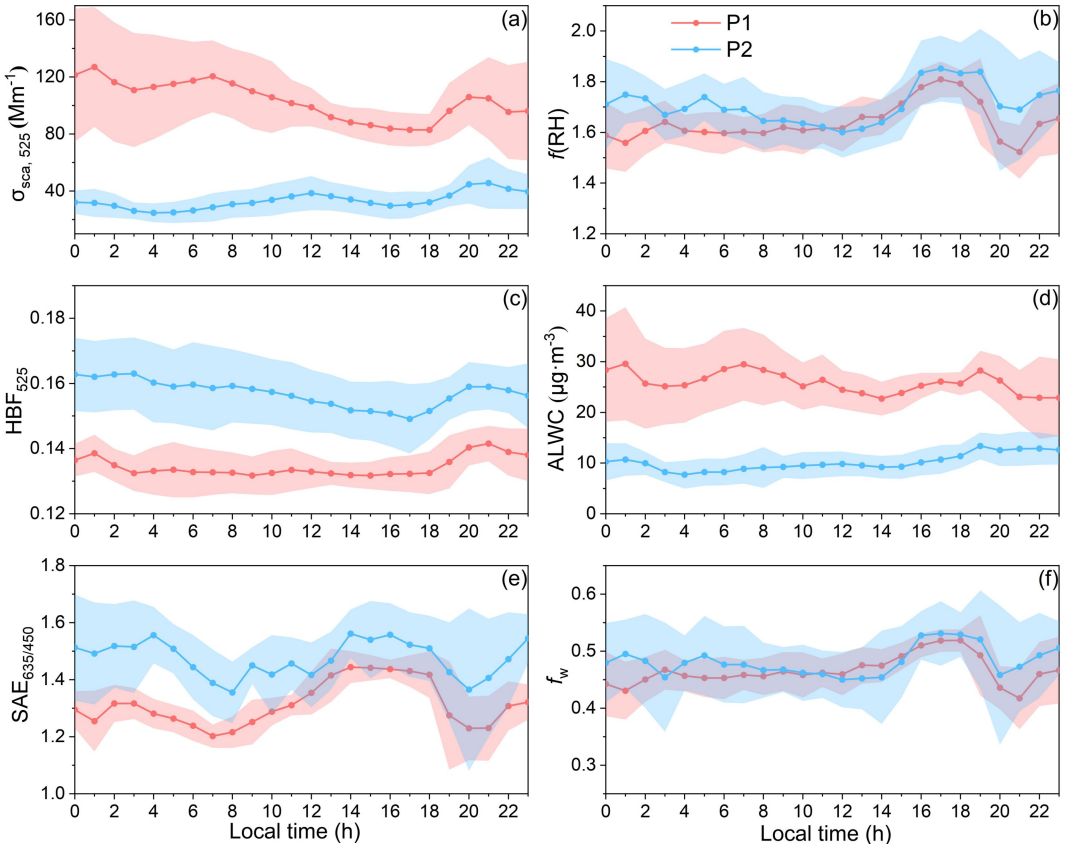

Figure 3. Diurnal variations of $\sigma_{sca,\ 525}$ **(a)**, *f*(RH) **(b)**, HBF_{525} **(c)**, ALWC **(d)**, $SAE_{635/450}$ **(e)** and f_W **(f)** on NPF days during P1 (red line) and P2 (blue line) periods. The shaded areas stand for the corresponding ± 1σ standard deviations.

Both HBF and SAE on P2 $NPF_{clean,\ HW}$ days were significantly higher than that of P1 $NPF_{polluted}$ cases (Fig. 3c, e), largely due to the smaller R_{eff} observed during heatwave-dominated period (Table S2). Moreover, the correlation between HBF (or SAE) and particle size in each mode was weaker on NPF days than on non-event days, especially for $NPF_{clean,\ HW}$ days (Fig. S14). A strongest negative correlation was found between HBF and R_{eff} of the accumulation mode in comparison to other modes, highlighting that HBF is more sensitive to the size distribution of accumulation mode particles (Collaud Coen et al., 2007). Given that NPF would largely enhance the abundance of both nucleation and Aitken mode aerosols (Fig. S7), no significant

variation in HBF was observed during the daytime due to the weakened correlation between HBF and $R_{Acc.}$ of NPF events. SAE is commonly used as an indicator of particle size distribution, almost decreasing monotonously with the increase of aerosol size within 1 μm (Kuang et al., 2017, 2018; Luoma et al., 2019). Accordingly, SAE decreased over the morning and evening rush hours when coarse particles (e.g., aged particles, road dust, automobile exhaust) generated during anthropogenic activities, accompanied with an increase in CO that is taken as the proxy for primary emissions (Fig. 2l) (Yarragunta et al., 2020). On the contrary, the abundant ultrafine particles formed during NPF events led to a continuous increase in SAE during the day.

f(RH) exhibited a similar diurnal pattern on the P1 and P2 NPF days (Fig. 3b). During the daytime, *f*(RH) remained relatively stable and gradually increased until peaking around 16:00-18:00 LT, with a generally higher *f*(RH) particularly after 15:00 LT during P2 $NPF_{clean, HW}$ days than that of P1 cases. The insignificant fluctuation of relatively lower *f*(RH) levels before the noon could be attributed to the continuous development of the mixing layer (Fig. 2k), leading to an efficient mixing of particles in the nocturnal residual layer with anthropogenic emissions near the ground. Additionally, photochemical reactions in the afternoon facilitated the formation of more hygroscopic secondary aerosols with a higher oxidation level (Liu et al., 2014; R. Zhang et al., 2015). The diurnal patterns of O_3 and the O_3/O_X ratio (i.e., an indicator of atmospheric oxidation capacity, where $O_X = O_3 + NO_2$, Tian et al., 2021) also showed similar trends (Fig. 2g, 2h). The presence of black carbon (BC) mixed with organic compounds (e.g., from traffic emissions and residential cooking activities) explained the rapid decrease in *f*(RH) during the evening rush hours (Liu et al., 2011). Furthermore, the daily mean *f*(RH) for NPF days was higher than that of non-event days (Table S2), particularly after the ending of NPF events around 12:00 LT. Given that newly formed particles were too small to significantly impact the total light scattering (Fig. S11a), this indicates that the atmospheric conditions conducive to the occurrence of NPF may promote further growth (e.g., via photooxidation or atmospheric aging processes) of pre-existing particles and newly formed ones, leading to enhanced aerosol optical hygroscopicity as clued from the concurrent variations of

ALWC and f_W in urban Chongqing during hot summer (Asmi et al., 2010; Wang et al., 2019; Wu et al., 2016). The diurnal pattern of ALWC closely mirrored the variation in $\sigma_{sca,\ 525}$, while f_W followed the similar evolution of f(RH). This suggests that ALWC was more sensitive to changes in the aerosol volume concentration, as determined by the corresponding retrieval algorithm (Kuang et al., 2018). The f_W levels were slightly higher during NPF days in comparison to that of non-event days (Table S2). This difference was more pronounced in the afternoon of NPF days (e.g., even exceeded 50%; Fig. 3f), verified the enhancement of aerosol hygroscopicity during the subsequent growth and atmospheric aging of both pre-existing and newly formed particles.

3.4 Heatwave-induced divergent changes in aerosol optical hygroscopicity

To further explore the impacts of heatwaves on f(RH) during diverse NPF events, data mainly within the time window of 08:00-22:00 LT (i.e., typically covered the complete process of NPF and subsequent growth, while excluded higher RH conditions at night) were utilized for the following discussion.

Although ultrafine particles exhibited higher number concentrations during the study period, accumulation mode particles dominated the aerosol volume concentration and contributed predominantly to the total light scattering (Figs. S7, S13). A positive correlation between f(RH), R_{eff} and the volume fraction of accumulation mode particles ($VF_{Acc.}$) was found on non-event days (Fig. 4c-d), when the aerosol size distribution was undisturbed by newly formed ultrafine particles and the corresponding $VF_{Acc.}$ maintained around a high level of 0.95 (Fig. 4a-b). The notably positive correlation between f(RH) and R_{eff} could be linked to the secondary formation of hygroscopic particles within the accumulation mode, primarily via photochemical reactions and further intensified by heatwaves during the non-event day particularly of the P2 period (Gu et al., 2023; Liu et al., 2014; R. Zhang et al., 2015; Zhang et al., 2024). Consequently, f(RH) at a specific R_{eff} was generally higher during the P2 period in comparison to that of P1 (Fig. 4c-d), also with high f(RH) levels observed for smaller size cases of R_{eff} <110 nm under some extremely high

temperature conditions (T >40 ℃, as highlighted by the red dashed circle in Fig. 4d). The higher SOC/OC on P2 non-event days further demonstrated the stronger secondary aerosol formation in comparison to P1 non-event days (Fig. S3b).

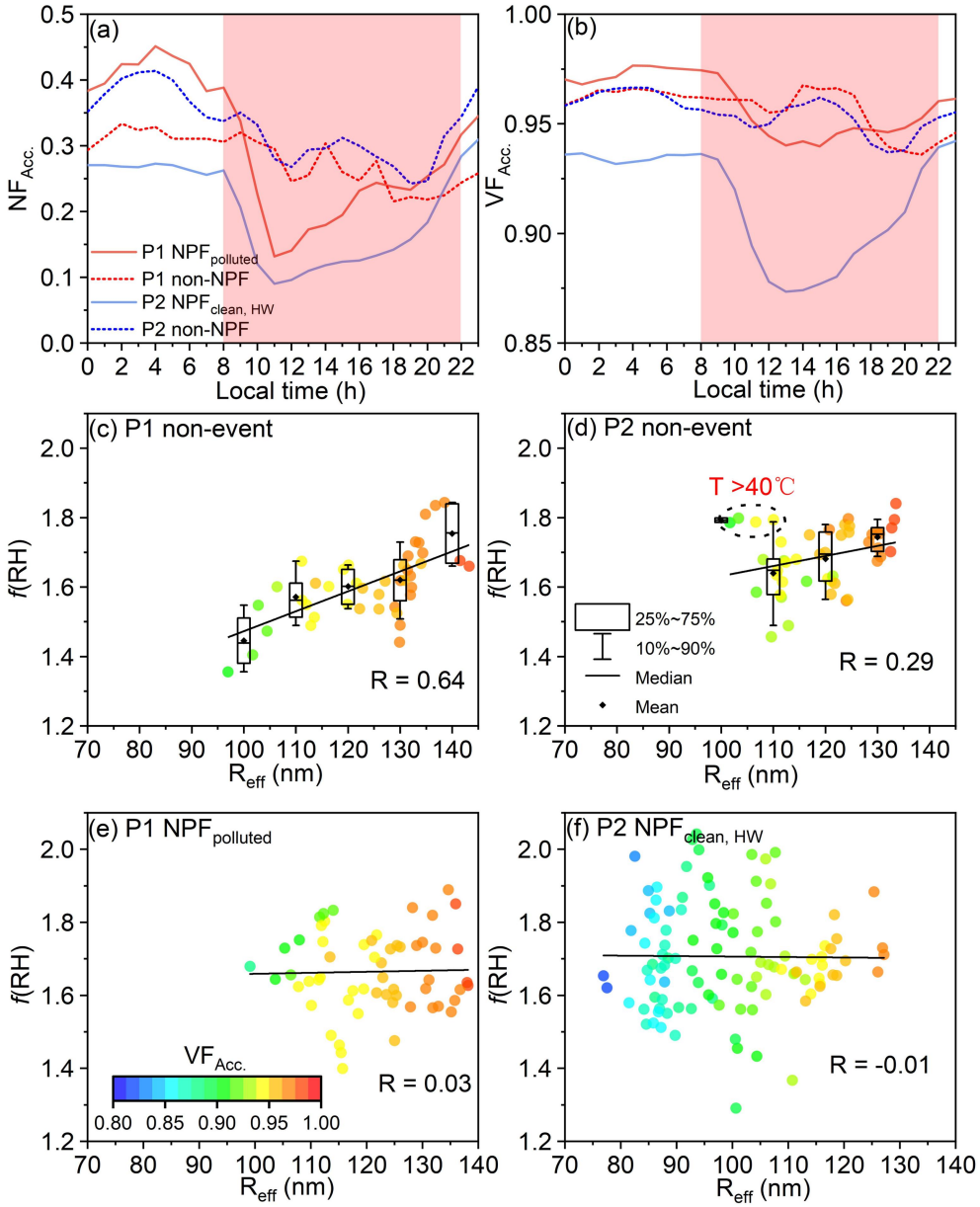

Figure 4. Diurnal variations of **(a)** the number fraction ($NF_{Acc.}$) and **(b)** volume fraction of accumulation mode particles ($VF_{Acc.}$) on P1 (red) and P2 (blue) NPF days (solid line), as well as non-event days (dash line). The time window of 08:00-22:00 LT was shaded in red. The relationship of *f*(RH) with R_{eff} and $VF_{Acc.}$ (as indicated by the colored dots) on P1 **(c)** and P2 non-event days **(d)**, as well as on P1 **(e)** and P2 **(f)** NPF days during the 08:00-22:00 LT time window.

Nevertheless, *f*(RH) was almost independent of the two parameters (i.e., R_{eff} and $VF_{Acc.}$) for NPF events (Fig. 4e-f). This is mainly due to the explosive formation of ultrafine particles and subsequent growth on NPF days, significantly altering aerosol size distributions and inducing large fluctuations in the number and volume fractions of accumulation mode particles (as shaded in Fig. 4a-b). Therefore, characterizing *f*(RH) with the corresponding R_{eff} of aerosol populations was no longer applicable. Alternatively, SAE was commonly used to estimate or parameterize *f*(RH) (Titos et al., 2014; Xia et al., 2023; Xue et al., 2022), in line with the similar diurnal patterns of *f*(RH) and SAE observed in this study. Figure 5 demonstrated a significantly positive correlation between *f*(RH) and SAE during NPF days in comparison to non-event days, with a similar slope of approximately 0.65 suggesting the consistent variation of *f*(RH) with SAE across both periods. As larger particles contributed higher to the aerosol volume concentrations (Fig. S5), the decrease of SAE also corresponded to an increase in $\sigma_{sca,\ 525}$ (Fig. 5a3, b3). Given that larger $\sigma_{sca,\ 525}$ values typically indicate the condition of a higher aerosol loading, *f*(RH) increased with SAE whereas decreased with $\sigma_{sca,\ 525}$, or rather the pollution level, during NPF days. The cleaner environment of P2 period may further favor the occurrence of NPF events. Both *f*(RH) and SAE exhibited a higher level on P2 $NPF_{clean,\ HW}$ days (as shown by the dash lines in Fig. 5), likely attributed to the following two aspects. One is related to the smaller aerosol R_{eff} (with a larger SAE) due to the lower FR and GR, likely influenced by the evaporation of newly-formed unstable clusters and particle coatings under heatwaves (Bousiotis et al., 2021; Cusack et al., 2013; Deng et al., 2020) during the subsequent growth of aerosols. Secondly, the higher temperature was normally associated with stronger photochemical oxidation, which could intensify the formation of secondary aerosol components with a higher hygroscopicity (Asmi et al., 2010; Gu et al., 2023; Liu et al., 2014; Wu et al., 2016; R. Zhang et al., 2015; Zhang et al., 2024). This is further supported by the slightly higher levels of UVB (P1: 2.6 ± 1.9 $W \cdot m^{-2}$ versus P2: 2.7 ± 2.0 $W \cdot m^{-2}$) and O_3/O_X (P1: 0.81 ± 0.17 versus P2: 0.82 ± 0.17) during P2 heatwave days, also in line with a recent study which demonstrated that heatwaves affected

secondary organic aerosols (SOA) formation and aging by accelerating photooxidation in Beijing (Zhang et al., 2024).

It is worth noting that *f*(RH) did not show a consistently higher level after the $NPF_{clean,\ HW}$ occurrence during P2 period, and it was slightly higher within the first few hours of NPF occurrence (i.e., ~ 12:00 -15:00 LT) on P1 $NPF_{polluted}$ days (Fig. 3b). In fact, aerosol optical hygroscopicity not fully corresponds to the bulk hygroscopicity primarily determined by aerosol chemical components, and the variability in aerosol optical features also plays a key role in *f*(RH). Hence, the size-dependency of aerosol optical properties should be considered. The size-resolved $\sigma_{sca,\ 525}$ distribution and size-resolved cumulative frequency distribution (CFD) of $\sigma_{sca,\ 525}$ over different NPF days were calculated using the Mie theory, with good agreements between the theoretically calculated and measured $\sigma_{sca,\ 525}$ values (R^2 = 0.99). As shown in Fig. S11a and Fig. S13, new particles must grow into the accumulation mode size at least before they can exert a significant influence on the total scattering coefficient. The critical sizes corresponding to the cumulative frequency of 50% in $\sigma_{sca,\ 525}$ were 358.7 nm and 333.8 nm on P1 and P2 NPF days, respectively. This indicates that relatively smaller particles including the newly formed and grown ones mixed with pre-existing and aged particles contributed a slightly higher portion to $\sigma_{sca,\ 525}$ on P2 $NPF_{clean,\ HW}$ days, while the $\sigma_{sca,\ 525}$ was mainly contributed by larger ones on P1 $NPF_{polluted}$ days. Nevertheless, the Mie theory suggests that these smaller particles generally have a weaker enhancement in total scattering after hygroscopic growth, in comparison to larger size particles (Collaud Coen et al., 2007, Fig. S11a). Consequently, the changes in aerosol optical and hygroscopic properties necessitate consideration of both aerosol optical and chemical characteristics during different NPF events. Newly formed ultrafine particles contributed minor to aerosol optical properties, resulting in a lower *f*(RH) during the initial hours of P2 $NPF_{clean,\ HW}$ events compared to that of P1 $NPF_{polluted}$ events (Fig. 3b), as evidenced by a smaller R_{eff} for P2 $NPF_{clean,\ HW}$ events (Fig. S6). In contrast, the growth of pre-existing and newly formed particles into larger sizes would subsequently affect bulk aerosol optical properties, which was evidenced by the enhancement in aerosol extinction coefficient observed after NPF

occurrence in a recent study (Sun et al., 2024). Specifically, particles could undergo a longer and more intensified photochemical aging process during $NPF_{clean, HW}$ events as influenced by persistent heatwaves, which facilitated the secondary formation of hygroscopic aerosols and resulted in a higher *f*(RH) after 15:00 LT (Fig. 3b).

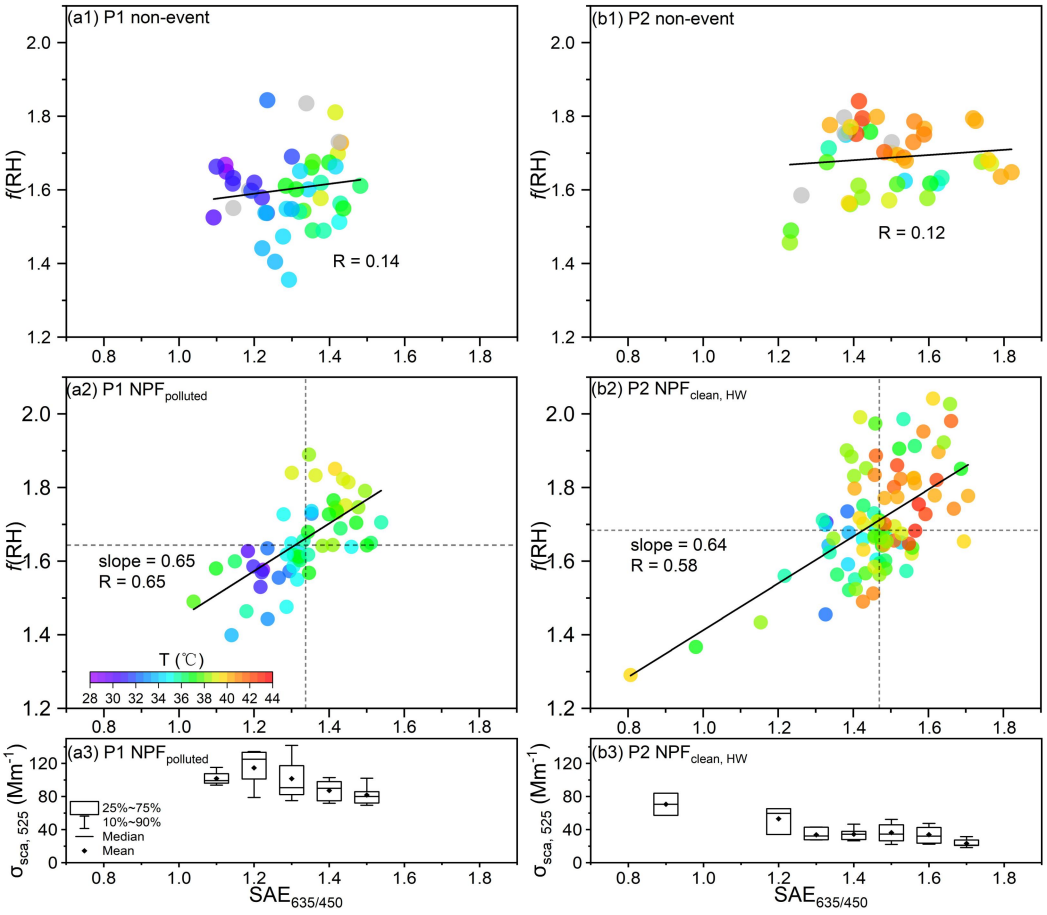

Figure 5. The relationship between *f*(RH) and $SAE_{635/450}$, as well as temperature (as indicated by the color of dots, missing values are represented in gray), on P1 non-event days **(a1)**, $NPF_{polluted}$ days **(a2)** during the 08:00-22:00 LT time window. The vertical (horizontal) dash line represents the median value of $SAE_{635/450}$ (*f*(RH)). **(a3)** The corresponding $\sigma_{sca, 525}$ under different $SAE_{635/450}$ levels on P1 $NPF_{polluted}$ days. **(b1-b3)** The same but for P2 period.

3.5 *f*(RH)-induced changes in aerosol direct radiative forcing

The changes in *f*(RH) have significant implications for aerosol direct radiative forcing. Despite considerably lower $\sigma_{sca, 525}$ results during heatwaves, the corresponding mean f_{RF}(RH) levels particularly for P2 $NPF_{clean, HW}$ days were higher

than that of the P1 cases (Fig. 6a). A robust positive correlation (R^2 = 0.68) was observed between f(RH) and aerosol radiative forcing enhancement factor, f_{RF}(RH) (Fig. 6b). This is likely attributed to the enhanced f_{RF}(RH) with the larger forward scattering ratio β, or rather higher HBF for smaller particle sizes, as supported by a generally negative correlation between f_{RF}(RH) and R_{eff}. Specifically, the highest f_{RF}(RH) value of 2.21 ± 0.23 was observed on P2 $NPF_{clean, HW}$ days, characterized with the highest f(RH) and smallest R_{eff} (i.e., highest HBF) of the entire study period.

The definition of f_{RF}(RH) in Eq.(5) implies the dependences of f_{RF}(RH) on both f(RH) and HBF-derived β(RH) and β(dry), or rather the ratio of $HBF_{525, RH}/HBF_{525}$. The mean $HBF_{525, RH}$ was generally larger than HBF_{525} in this study, specifically with the $HBF_{525, RH}/HBF_{525}$ ratios centered around 1.8 and even approached 2.5 on P2 $NPF_{clean, HW}$ days (Fig. 6c, Table S2). This could be different from the classical Mie theory with the spherical-particle premise, i.e., the observed light backscattering was enhanced after hydration likely resulted from the evolution in particle morphology that significantly influences their optical properties (Mishchenko 2009). Additionally, the predominant organic components when heterogeneously mixed with diverse chemical compositions (e.g., inorganics and black carbon) likely introduced the heterogeneity in aerosol hygroscopicity (Yuan and Zhao, 2023), which may alter particle morphology thereby optical properties upon water uptake (Giordano et al., 2015; Tan et al., 2020; Tritscher et al., 2011). The efficient evaporation of organic coatings under extremely hot conditions could also contribute to the change in particle morphology (e.g., non-spherical inregular shapes) upon humidification, as evidenced by a recent study that high temperature conditions could accelerate the evaporation rate of SOA (Li et al., 2019). Given that the backward scattering intensity of non-spherical particles is suggested to be much larger than its spherical counterparts at scattering angles between 90° and 150° (Mishchenko 2009; Yang et al., 2007) and that the HBF-derived asymmetry parameter (g) normally correlates positively with the aerosol forward scattering (Andrews et al., 2006; Marshall et al., 1995), the generally smaller g_{RH} results (in comparison to g) confirmed the decrease (increase) in the forward (backward) light scattering after water uptake (Fig. S11c), likely implying the

change in the morphological structure of particles. This is particularly evident for P2 $NPF_{clean,\ HW}$ days, with a much lower level of g_{RH} was observed (Fig. S11c). Another possible reason is the distinct size dependences of both light scattering and backscattering efficiencies (Fig. S11a), with much more significant enhancements in the backscattering efficiency thereby HBF specifically of accumulation mode particles after hygroscopic growth (Fig. S11b). As reflected by the Mie model, although the abundant newly formed particles were generally optically-insensitive (e.g., below 100 nm), their contributions to $\sigma_{sca,\ 525}$ and especially to $\sigma_{bsca,\ 525}$ could be amplified upon humidification (Fig. S11b). Besides, the shift of size distribution towards larger accumulation-mode particles could also result in a significant elevation in $HBF_{525,\ RH}/HBF_{525}$ ratios, especially under the condition of a smaller mode diameter and narrower distribution of ultrafine-mode particles (e.g., during NPF events) (Fig. S15a1-b2 for the theoretical sensitivity tests of Sect. S9 in the supplement). Furthermore, the $HBF_{525,\ RH}/HBF_{525}$ ratio exhibited a significant positive correlation with the real part of complex refractive index (*n*) of bulk aerosols (Fig. S16), and *n* tends to increase with the aging process of organic species (Moise et al., 2015; Zhao et al., 2021). In this sense, the evolution of both aerosol size distribution pattern and chemical compositions, combined with the heterogeneity in aerosol hygroscopicty, could potentially change particle morphology and optical properties (e.g., complex refractive index and elevated $HBF_{525,\ RH}$) particularly during heatwave-influenced $NPF_{clean,\ HW}$ days, characterized with the smallest aerosol R_{eff} (102.8 ± 12.4 nm) (Figure. S6), lowest number concentration (1897.0 ± 680.8 cm^{-3}) and fraction (0.20 ± 0.10) of accumulation mode particles, intensified photooxidation, and a higher SOC/OC ratio. The higher $HBF_{525,\ RH}/HBF_{525}$ ratios increased the HBF-derived β(RH)/β(dry) levels, in combination of the elevated *f*(RH), further resulting in the highest f_{RF}(RH) observed during P2 $NPF_{clean,\ HW}$ events. Given that previously observed $HBF_{525,\ RH}$ was typically lower than HBF_{525} (Titos et al., 2021; Xia et al., 2023; L. Zhang et al., 2015), the mean f_{RF}(RH) results of this study (f_{RF}(85%) = 2.05 ± 0.24) were significantly higher than those observed in the Yangtze River Delta (f_{RF}(85%) = 1.5, L. Zhang et al., 2015), the North China Plain (f_{RF}(80%) = 1.6 ± 0.2,

Xia et al., 2023), and some other regions in the world (Titos et al., 2021, Fig. 6d). It should be noted that the reported f_{RF}(RH) for the UGR site (Spain) was even higher, likely due to the higher R_s and α_s used in the derivation of f_{RF}(RH) in that area (Titos et al., 2021).

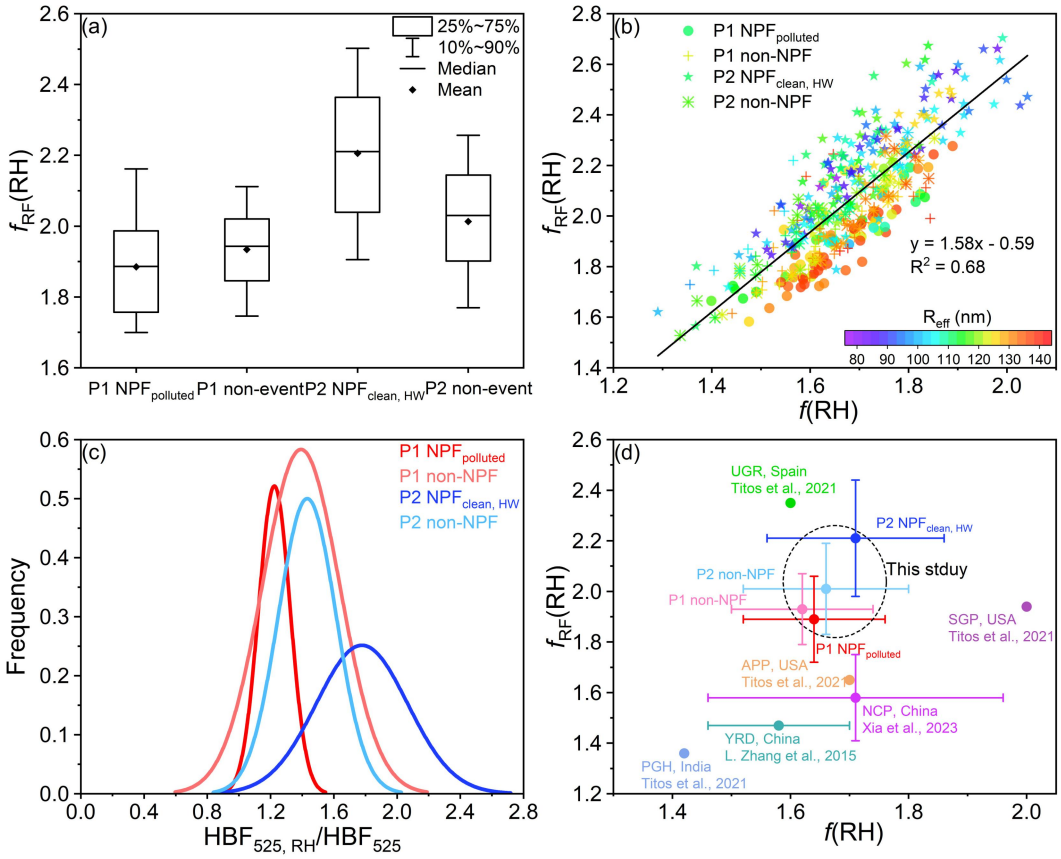

Figure 6. (a) The box-plot of f_{RF}(RH) during P1 or P2 NPF event and non-event days. **(b)** The relationship between f_{RF}(RH) and f(RH), as colored by the corresponding R_{eff}, during P1 or P2 NPF and non-event days (shown in different symbols). **(c)** Occurrence frequency of the HBF$_{525, RH}$/HBF$_{525}$ ratios during P1 or P2 NPF and non-event days. **(d)** The mean f_{RF}(RH) under different f(RH) levels (the error bars stand for ± one standard deviations corresponding to f_{RF}(RH) and f(RH), respectively), along with the reported f_{RF}(RH) and f(RH) data for other regions in the world.

A recent study has indicated that continuous reduction of $PM_{2.5}$ mass loadings can increase the net solar radiation, thereby promoting NPF events (Zhao et al., 2021). Given the complexity and dynamic evolution of the atmospheric environment, these can further alter the intrinsic properties of aerosol particles (e.g., f(RH), HBF,

morphology), potentially feeding back into aerosol-radiation interactions. Our findings suggest that NPF and growth events may elevate aerosol optical hygroscopicity in rather hot environments, e.g., the Basin area and tropical regions. Meanwhile, NPF serves as a crucial secondary transformation process in the atmosphere (Zhu et al., 2021). The favorable atmospheric diffusion capability ensured the mixing of newly formed particles into the upper boundary layer, where is colder and more humid than that near the surface during heatwaves (Jin et al., 2022). Hence, the enhancement of aerosol optical hygroscopicity during the subsequent growth of pre-existing and newly formed particles possibly exacerbates secondary pollution and even triggers haze events (Hao et al., 2024; Kulmala et al., 2021). On the other hand, a large number of studies have demonstrated that the new particles of higher hygroscopicity could contribute more to the activation of CCN (Ma et al., 2016; Ren et al., 2021; Rosati et al., 2022; Sun et al., 2024; Wu et al., 2015), thereby modulating the aerosol-cloud interactions and further the global climate (Fan et al., 2016; Merikanto et al., 2006; Westervelt et al., 2013). Additionally, the simultaneous decrease in aerosol effective radius and possibly evaporation-induced non-spherical particle morphology further enhance the aerosol direct radiative forcing enhancement factor, potentially amplifying the cooling effect mainly caused by light scattering aerosols. This highlights the needs for further in-depth exploration on aerosol radiative impacts at weather extremes (e.g., heatwaves) with the changing climate, given the continuous reductions of anthropogenic emissions and more intense emissions of biogenic origins with the global warming. Besides, more detailed information on the evolution of particle morphology with the changing environment (e.g., varied temperature and RH) would enrich insights into the aerosol radiative forcing.

4 Conclusions and implications

A rare heatwave event raged throughout urban Chongqing of southwest China in the summer of 2022, which significantly influenced aerosol physicochemical properties and atmospheric processes (e.g., NPF and subsequent growth). Concurrent measurements of aerosol optical and hygroscopic properties, PNSD, and bulk chemical compositions were conducted to explore the mechanisms behind the variations in aerosol optical hygroscopicity during different NPF days under diverse weather conditions.

NPF events exhibited distinct characteristics during the normally hot (P1, relatively polluted) and heatwaves-dominated (P2, quite clean) periods. $NPF_{polluted}$ within P1 period was favored by the decrease in background aerosol loading and the higher abundance of H_2SO_4. $NPF_{clean,\ HW}$ events that occurred during the heatwave P2 period were characterized with lower CS, CoagS, FR and GR, as well as smaller R_{eff} and D_{mode}, than P1 $NPF_{polluted}$ cases. In comparison to the P1 $NPF_{polluted}$ events, $NPF_{clean,\ HW}$ occurred approximately one hour earlier and the subsequent growth was longer during P2, likely intensifying the photochemical oxidation due to heatwave-influenced aging processes and modulating the evolution of aerosol size distributions differently. Furthermore, significant differences in aerosol optical and hygroscopic properties were observed between the normally hot and heatwave-dominated NPF days. The newly formed and grown particles mixed with pre-existing aerosols contributed a minor $\sigma_{sca,\ 525}$ noontime peak occurred on the much cleaner P2 $NPF_{clean,\ HW}$ days, while the $\sigma_{sca,\ 525}$ peaked earlier around the morning rush hours on P1 $NPF_{polluted}$ days. HBF and SAE were significantly higher on P2 $NPF_{clean,\ HW}$ days, primarily due to the smaller R_{eff} for heatwave-influenced $NPF_{clean,\ HW}$ cases. f(RH) remained relatively stable during the daytime of NPF days and peaked around 16:00-18:00 LT. Specifically, aerosol optical hygroscopicity tended to be higher during the subsequent growth and aging of both pre-existing particles and newly formed ones on P2 $NPF_{clean,\ HW}$ days than that for P1 $NPF_{polluted}$ days, which aligned with the higher f_W levels.

Compared with non-event cases, the generally higher levels of daily mean f(RH) suggested that the aerosol optical hygroscopicity was enhanced on NPF days in hot summer of urban Chongqing. A significantly positive (negative) correlation between f(RH) and SAE ($\sigma_{sca,\ 525}$, or rather the pollution level) was observed on NPF days for both periods, accompanied by higher f(RH) and SAE values on $NPF_{clean,\ HW}$ days. This was likely due to the evaporation of both unstable clusters and particle coatings under heatwaves (Bousiotis et al., 2021; Cusack et al., 2013; Deng et al., 2020; Garmash et al., 2024), thereby reducing aerosol sizes (e.g., R_{eff}, D_{mode}) whereas increasing SAE. Moreover, heatwave-influenced stronger photooxidation enhanced the formation of more hygroscopic secondary components during the subsequent growth/aging processes of both pre-existing and newly formed particles on P2 $NPF_{clean,\ HW}$ days in comparison to that of P1 $NPF_{polluted}$ cases. The aerosol light scattering or volume concentration was mainly contributed by the larger accumulation-mode particles, while more ultrafine particles dominated the size distribution especially for the initial stage of heatwave-influenced $NPF_{clean,\ HW}$ events, further leading to a lower f(RH) following the NPF occurrence (i.e., ~ 12:00 -15:00 LT) in comparison to P1 $NPF_{polluted}$ days.

Changes in f(RH) could potentially impact the aerosol direct radiative forcing. A robust positive (negative) correlation existed between f_{RF}(RH) and f(RH) (R_{eff}). Despite a lower $\sigma_{sca,\ 525}$ during heatwaves, the corresponding mean f_{RF}(RH) was relatively higher and the maximum value of 2.21 ± 0.23 was observed on P2 $NPF_{clean,\ HW}$ days, associated with the highest f(RH) (1.71 ± 0.13), smallest R_{eff} (102.8 ± 12.4 nm), and highest $HBF_{525,\ RH}/HBF_{525}$ ratios (1.78 ± 0.29). The above highlights that heatwaves could influence the NPF (e.g., the evolution in the aerosol size distribution pattern and chemical composition) and atmospheric processing (although with a decreased aerosol R_{eff} and D_{mode} likely due to evaporation-resulted non-spherical particle morphology under persistently high temperature conditions), thereby enhancing aerosol optical hygroscopic growth and potentially reducing the net solar radiation directly especially in hot summer. Further explorations on detailed molecular-scale characterizations (e.g., molecular structures and compositions of

729 newly and secondary formed particles, as well as particle morphology) and aerosol
730 radiative impacts including the aerosol-cloud interactions of weather extremes (e.g.,
731 heatwaves) with the changing climate are highly recommended.
732
733 **Data availability.** Data will be available upon request.
734
735 **Author contributions.** YH and PL: Methodology, Investigation, Data analysis,
736 Formal analysis, Visualization, Validation, Writing – original draft & editing. YG and
737 ZW: Methodology, Investigation, Formal analysis. MT, YC, HX and WH: Data
738 curation, Methodology. FW and YL: Investigation. YK: Methodology, Data analysis,
739 Writing – review & editing. JC: Conceptualization, Methodology, Funding acquisition,
740 Data curation, Writing – review & editing, Supervision.
741
742 **Competing interests.** The authors declare no competing financial interest.
743
744 **Acknowledgement.** This work was supported by the National Natural Science
745 Foundation of China (No. 42105075), Venture and Innovation Support Program
746 for Chongqing Overseas Returnees (No. cx2021021). We thank Biao Xue for the
747 technical support on the utilization and maintenance of the humidified
748 nephelometer system. We also thank Ziqian Wang for the TSP filter sample
749 collection and Jiawei Zhou for the corresponding offline chemical analysis.
750
751 **References**
752 An, J., Lu, Y., Huang, D. D., Ding, X., Hu, Q., Yan, R., Qiao, L., Zhou, M., Huang, C.,
753 Wang, H., Fu, Q., Yu, F., and Wang, L.: Sectoral Size - Resolved Particle Number
754 Emissions With Speciation: Emission Profile - Based Quantification and a Case Study

in the Yangtze River Delta Region, China, J. Geophys. Res. Atmos., 1–22, https://doi.org/10.1029/2024JD041234, 2024.

Andrews, E., Sheridan, P. J., Fiebig, M., McComiskey, A., Ogren, J. A., Arnott, P., Covert, D., Elleman, R., Gasparini, R., Collins, D., Jonsson, H., Schmid, B., and Wang, J.: Comparison of methods for deriving aerosol asymmetry parameter, J. Geophys. Res. Atmos., 111, 1–16, https://doi.org/10.1029/2004JD005734, 2006.

Asmi, E., Frey, A., Virkkula, A., Ehn, M., Manninen, H. E., Timonen, H., Tolonen-Kivimäki, O., Aurela, M., Hillamo, R., and Kulmala, M.: Hygroscopicity and chemical composition of antarctic sub-micrometre aerosol particles and observations of new particle formation, Atmos. Chem. Phys., 10, 4253–4271, https://doi.org/10.5194/acp-10-4253-2010, 2010.

Bae, M. S., Lee, T., Schauer, J. J., Park, G., Son, Y. B., Kim, K. H., Cho, S. S., Park, S. S., Park, K., and Shon, Z. H.: Chemical Characteristics of Size-Resolved Aerosols in Coastal Areas during KORUS-AQ Campaign; Comparison of Ion Neutralization Model, Asia-Pacific J. Atmos. Sci., 55, 387–399, https://doi.org/10.1007/s13143-018-00099-1, 2019.

Bousiotis, D., Brean, J., Pope, F. D., Dall'Osto, M., Querol, X., Alastuey, A., Perez, N., Petäjä, T., Massling, A., Klenø Nøjgaard, J., Nordstrøm, C., Kouvarakis, G., Vratolis, S., Eleftheriadis, K., Niemi, J. V., Portin, H., Wiedensohler, A., Weinhold, K., Merkel, M., Tuch, T., and Harrison, R. M.: The effect of meteorological conditions and atmospheric composition in the occurrence and development of new particle formation (NPF) events in Europe, Atmos. Chem. Phys., 21, 3345–3370, https://doi.org/10.5194/acp-21-3345-2021, 2021.

Brooke Anderson, G. and Bell, M. L.: Heat waves in the United States: Mortality risk during heat waves and effect modification by heat wave characteristics in 43 U.S. communities, Environ. Health Perspect., 119, 210–218, https://doi.org/10.1289/ehp.1002313, 2011.

Cai, R., Chandra, I., Yang, D., Yao, L., Fu, Y., Li, X., Lu, Y., Luo, L., Hao, J., Ma, Y., Wang, L., Zheng, J., Seto, T., and Jiang, J.: Estimating the influence of transport on aerosol size distributions during new particle formation events, Atmos. Chem. Phys., 18, 16587–16599, https://doi.org/10.5194/acp-18-16587-2018, 2018.

Chen, J., Zhao, C. S., Ma, N., and Yan, P.: Aerosol hygroscopicity parameter derived from the light scattering enhancement factor measurements in the North China Plain, Atmos. Chem. Phys., 14, 8105–8118, https://doi.org/10.5194/acp-14-8105-2014, 2014.

Chen, Q., Mu, Z., Song, W., Wang, Y., Yang, Z., Zhang, L., and Zhang, Y. L.: Size-Resolved Characterization of the Chromophores in Atmospheric Particulate Matter From a Typical Coal-Burning City in China, J. Geophys. Res. Atmos., 124, 10546–10563, https://doi.org/10.1029/2019JD031149, 2019.

Chen, T., Wang, T., Xue, L., and Brasseur, G.: Heatwave exacerbates air pollution in China through intertwined climate-energy-environment interactions, Sci. Bull., 69, 2765–2775, https://doi.org/10.1016/j.scib.2024.05.018, 2024.

China Meteorological Administration, 2022. China Climate Bulletin 2022. https://www.cma.gov.cn/zfxxgk/gknr/qxbg/202303/t20230324_5396394.html. Accessed on 23 March 2023. (in Chinese).

Cho Cheung, H., Chung-Kuang Chou, C., Siu Lan Lee, C., Kuo, W. C., and Chang, S. C.: Hygroscopic properties and cloud condensation nuclei activity of atmospheric aerosols under the influences of Asian continental outflow and new particle formation at a coastal site in eastern Asia, Atmos. Chem. Phys., 20, 5911–5922, https://doi.org/10.5194/acp-20-5911-2020, 2020.

Chylek, P. and Wong, J.: Effect of absorbing aerosols on global radiation budget, Geophys. Res. Lett., 22, 929–931, https://doi.org/10.1029/95GL00800, 1995.

807 Collaud Coen, M., Weingartner, E., Nyeki, S., Cozic, J., Henning, S., Verheggen, B.,
808 Gehrig, R., and Baltensperger, U.: Long-term trend analysis of aerosol variables at the
809 high-alpine site Jungfraujoch, J. Geophys. Res. Atmos., 112,
810 https://doi.org/10.1029/2006JD007995, 2007.

811 Covert, D. S., Charlson, R. J., and Ahlquist, N. C.: A Study of the Relationship of
812 Chemical Composition and Humidity to Light Scattering by Aerosols, J. Appl.
813 Meteorol., 11, 968–976,
814 https://doi.org/10.1175/1520-0450(1972)011<0968:asotro>2.0.co;2, 1972.

815 Crumeyrolle, S., Kontkanen, J. S. S., Rose, C., Velazquez Garcia, A., Bourrianne, E.,
816 Catalfamo, M., Riffault, V., Tison, E., Ferreira De Brito, J., Visez, N., Ferlay, N.,
817 Auriol, F., and Chiapello, I.: Measurement report: Atmospheric new particle
818 formation at a peri-urban site in Lille, northern France, Atmos. Chem. Phys., 23,
819 183–201, https://doi.org/10.5194/acp-23-183-2023, 2023.

820 Cusack, M., Alastuey, A., and Querol, X.: Case studies of new particle formation and
821 evaporation processes in the western Mediterranean regional background, Atmos.
822 Environ., 81, 651–659, https://doi.org/10.1016/j.atmosenv.2013.09.025, 2013.

823 Dada, L., Paasonen, P., Nieminen, T., Buenrostro Mazon, S., Kontkanen, J., Peräkylä,
824 O., Lehtipalo, K., Hussein, T., Petäjä, T., Kerminen, V. M., Bäck, J., and Kulmala, M.:
825 Long-term analysis of clear-sky new particle formation events and nonevents in
826 Hyytiälä, Atmos. Chem. Phys., 17, 6227–6241,
827 https://doi.org/10.5194/acp-17-6227-2017, 2017.

828 Dal Maso, M., Kulmala, M., Riipinen, I., Wagner, R., Hussein, T., Aalto, P. P., and
829 Lehtinen, K. E. J.: Formation and growth of fresh atmospheric aerosols: Eight years
830 of aerosol size distribution data from SMEAR II, Hyytiälä, Finland, Boreal Environ.
831 Res., 10, 323–336, 2005.

Delene, D. J. and Ogren, J. A.: Variability of aerosol optical properties at four North American surface monitoring sites, J. Atmos. Sci., 59, 1135–1150, https://doi.org/10.1175/1520-0469(2002)059<1135:VOAOPA>2.0.CO;2, 2002.

Deng, C., Cai, R., Yan, C., Zheng, J., and Jiang, J.: Formation and growth of sub-3 nm particles in megacities: Impact of background aerosols, Faraday Discuss., 226, 348–363, https://doi.org/10.1039/d0fd00083c, 2021.

Deng, C., Fu, Y., Dada, L., Yan, C., Cai, R., Yang, D., Zhou, Y., Yin, R., Lu, Y., Li, X., Qiao, X., Fan, X., Nie, W., Kontkanen, J., Kangasluoma, J., Chu, B., Ding, A., Kerminen, V. M., Paasonen, P., Worsnop, D. R., Bianchi, F., Liu, Y., Zheng, J., Wang, L., Kulmala, M., and Jiang, J.: Seasonal characteristics of new particle formation and growth in urban Beijing, Environ. Sci. Technol., 54, 8547–8557, https://doi.org/10.1021/acs.est.0c00808, 2020.

Duan, J., Huang, R. J., Wang, Y., Xu, W., Zhong, H., Lin, C., Huang, W., Gu, Y., Ovadnevaite, J., Ceburnis, D., and O'Dowd, C.: Measurement report: Size-resolved secondary organic aerosol formation modulated by aerosol water uptake in wintertime haze, Atmos. Chem. Phys., 24, 7687–7698, https://doi.org/10.5194/acp-24-7687-2024, 2024.

Fan, J., Wang, Y., Rosenfeld, D., and Liu, X.: Review of aerosol-cloud interactions: Mechanisms, significance, and challenges, J. Atmos. Sci., 73, 4221–4252, https://doi.org/10.1175/JAS-D-16-0037.1, 2016.

Fierz-Schmidhauser, R., Zieger, P., Gysel, M., Kammermann, L., Decarlo, P. F., Baltensperger, U., and Weingartner, E.: Measured and predicted aerosol light scattering enhancement factors at the high alpine site Jungfraujoch, Atmos. Chem. Phys, 10, 2319–2333, 2010.

Garmash, O., Ezhova, E., Arshinov, M., Belan, B., Lampilahti, A., Davydov, D., Räty, M., Aliaga, D., Baalbaki, R., Chan, T., Bianchi, F., Kerminen, V. M., Petäjä, T., and

Kulmala, M.: Heatwave reveals potential for enhanced aerosol formation in Siberian boreal forest, Environ. Res. Lett., 19, https://doi.org/10.1088/1748-9326/ad10d5, 2024.

Giordano, M., Espinoza, C., and Asa-Awuku, A.: Experimentally measured morphology of biomass burning aerosol and its impacts on CCN ability, Atmos. Chem. Phys., 15, 1807–1821, https://doi.org/10.5194/acp-15-1807-2015, 2015.

Gu, Y., Huang, R. J., Duan, J., Xu, W., Lin, C., Zhong, H., Wang, Y., Ni, H., Liu, Q., Xu, R., Wang, L., and Li, Y. J.: Multiple pathways for the formation of secondary organic aerosol in the North China Plain in summer, Atmos. Chem. Phys., 23, 5419–5433, https://doi.org/10.5194/acp-23-5419-2023, 2023.

Guenther, A. B., Monson, R. K., and Fall, R.: Isoprene and monoterpene emission rate variability: Observations with eucalyptus and emission rate algorithm development, J. Geophys. Res. Atmos., 96, 10799–10808, https://doi.org/10.1029/91jd00960, 1991.

Guo, X., Huang, J., Luo, Y., Zhao, Z., and Xu, Y.: Projection of heat waves over China for eight different global warming targets using 12 CMIP5 models, Theor. Appl. Climatol., 128, 507–522, https://doi.org/10.1007/s00704-015-1718-1, 2016.

Hamed, A., Joutsensaari, J., Mikkonen, S., Sogacheva, L., Dal Maso, M., Kulmala, M., Cavalli, F., Fuzzi, S., Facchini, M. C., Decesari, S., Mircea, M., Lehtinen, K. E. J., and Laaksonen, A.: Nucleation and growth of new particles in Po Valley, Italy, Atmos. Chem. Phys., 7, 355–376, https://doi.org/10.5194/acp-7-355-2007, 2007.

Hamed, A., Korhonen, H., Sihto, S. L., Joutsensaari, J., Jrvinen, H., Petäjä, T., Arnold, F., Nieminen, T., Kulmala, M., Smith, J. N., Lehtinen, K. E. J., and Laaksonen, A.: The role of relative humidity in continental new particle formation, J. Geophys. Res. Atmos., 116, 1–12, https://doi.org/10.1029/2010JD014186, 2011.

Hand, J. L. and Malm, W. C.: Review of aerosol mass scattering efficiencies from ground-based measurements since 1990, J. Geophys. Res. Atmos., 112, https://doi.org/10.1029/2007JD008484, 2007.

Hao, Y., Gou, Y., Wang, Z., Huang, W., Wan, F., Tian, M., and Chen, J.: Current challenges in the visibility improvement of urban Chongqing in Southwest China: From the perspective of PM2.5-bound water uptake property over 2015–2021, Atmos. Res., 300, 107215, https://doi.org/10.1016/j.atmosres.2023.107215, 2024.

Hao, Z., Chen, Y., Feng, S., Liao, Z., An, N., and Li, P.: The 2022 Sichuan-Chongqing spatio-temporally compound extremes: a bitter taste of novel hazards, Sci. Bull., 68, 1337–1339, https://doi.org/10.1016/j.scib.2023.05.034, 2023.

Hauser, M., Orth, R., and Seneviratne, S. I.: Role of soil moisture versus recent climate change for the 2010 heat wave in western Russia, Geophys. Res. Lett., 43, 2819–2826, https://doi.org/10.1002/2016GL068036, 2016.

Jefferson, A., Hageman, D., Morrow, H., Mei, F., and Watson, T.: Seven years of aerosol scattering hygroscopic growth measurements from SGP: Factors influencing water uptake, J. Geophys. Res. Atmos., 122, 9451–9466, https://doi.org/10.1002/2017JD026804, 2017.

Jin, X., Li, Z., Wu, T., Wang, Y., Cheng, Y., Su, T., Wei, J., Ren, R., Wu, H., Li, S., Zhang, D., and Cribb, M.: The different sensitivities of aerosol optical properties to particle concentration, humidity, and hygroscopicity between the surface level and the upper boundary layer in Guangzhou, China, Sci. Total Environ., 803, 150010, https://doi.org/10.1016/j.scitotenv.2021.150010, 2022.

Kerminen, V. M., Chen, X., Vakkari, V., Petäjä, T., Kulmala, M., and Bianchi, F.: Atmospheric new particle formation and growth: Review of field observations, Environ. Res. Lett., 13, https://doi.org/10.1088/1748-9326/aadf3c, 2018.

908 Kim, N., Yum, S. S., Park, M., Park, J. S., Shin, H. J., and Ahn, J. Y.: Hygroscopicity
909 of urban aerosols and its link to size-resolved chemical composition during spring and
910 summer in Seoul, Korea, Atmos. Chem. Phys., 20, 11245–11262,
911 https://doi.org/10.5194/acp-20-11245-2020, 2020.

912 Kotchenruther, R. A., Hobbs, P. V., and Hegg, D. A.: Humidification factors for
913 atmospheric aerosols off the mid-Atlantic coast of the United States, J. Geophys. Res.
914 Atmos., 104, 2239–2251, https://doi.org/10.1029/98JD01751, 1999.

915 Kuang, Y., He, Y., Xu, W., Zhao, P., Cheng, Y., Zhao, G., Tao, J., Ma, N., Su, H.,
916 Zhang, Y., Sun, J., Cheng, P., Yang, W., Zhang, S., Wu, C., Sun, Y., and Zhao, C.:
917 Distinct diurnal variation in organic aerosol hygroscopicity and its relationship with
918 oxygenated organic aerosol, Atmos. Chem. Phys., 20, 865–880,
919 https://doi.org/10.5194/acp-20-865-2020, 2020.

920 Kuang, Y., Zhao, C. S., Zhao, G., Tao, J. C., Xu, W., Ma, N., and Bian, Y. X.: A
921 novel method for calculating ambient aerosol liquid water content based on
922 measurements of a humidified nephelometer system, Atmos. Meas. Tech., 11,
923 2967–2982, https://doi.org/10.5194/amt-11-2967-2018, 2018.

924 Kuang, Y., Zhao, C., Tao, J., Bian, Y., Ma, N., and Zhao, G.: A novel method for
925 deriving the aerosol hygroscopicity parameter based only on measurements from a
926 humidified nephelometer system, Atmos. Chem. Phys., 17, 6651–6662,
927 https://doi.org/10.5194/acp-17-6651-2017, 2017.

928 Kulmala, M., Dada, L., Daellenbach, K. R., Yan, C., Stolzenburg, D., Kontkanen, J.,
929 Ezhova, E., Hakala, S., Tuovinen, S., Kokkonen, T. V., Kurppa, M., Cai, R., Zhou, Y.,
930 Yin, R., Baalbaki, R., Chan, T., Chu, B., Deng, C., Fu, Y., Ge, M., He, H., Heikkinen,
931 L., Junninen, H., Liu, Y., Lu, Y., Nie, W., Rusanen, A., Vakkari, V., Wang, Y., Yang, G.,
932 Yao, L., Zheng, J., Kujansuu, J., Kangasluoma, J., Petaja, T., Paasonen, P., Jarvi, L.,
933 Worsnop, D., Ding, A., Liu, Y., Wang, L., Jiang, J., Bianchi, F., and Kerminen, V. M.:
934 Is reducing new particle formation a plausible solution to mitigate particulate air

pollution in Beijing and other Chinese megacities?, Faraday Discuss., 226, 334–347, https://doi.org/10.1039/d0fd00078g, 2021.

Kulmala, M., Petäjä, T., Nieminen, T., Sipilä, M., Manninen, H. E., Lehtipalo, K., Dal Maso, M., Aalto, P. P., Junninen, H., Paasonen, P., Riipinen, I., Lehtinen, K. E. J., Laaksonen, A., and Kerminen, V. M.: Measurement of the nucleation of atmospheric aerosol particles, Nat. Protoc., 7, 1651–1667, https://doi.org/10.1038/nprot.2012.091, 2012.

Kulmala, M.: How Particles Nucleate and Grow, Science, 302, 1000–1001, https://doi.org/10.1126/science.1090848, 2003.

Kurtén, T., Torpo, L., Ding, C. G., Vehkamäki, H., Sundberg, M. R., Laasonen, K., and Kulmala, M.: A density functional study on water-sulfuric acid-ammonia clusters and implications for atmospheric cluster formation, J. Geophys. Res. Atmos., 112, 1–7, https://doi.org/10.1029/2006JD007391, 2007.

Lee, K., Chandra, I., Seto, T., Inomata, Y., Hayashi, M., Takami, A., Yoshino, A., and Otani, Y.: Aerial observation of atmospheric nanoparticles on Fukue Island, Japan, Aerosol Air Qual. Res., 19, 981–994, https://doi.org/10.4209/aaqr.2018.03.0077, 2019.

Li, Y., Ding, Y., and Li, W.: Observed trends in various aspects of compound heat waves across China from 1961 to 2015, J. Meteorol. Res., 31, 455–467, https://doi.org/10.1007/s13351-017-6150-2, 2017.

Li, Z., Tikkanen, O. P., Buchholz, A., Hao, L., Kari, E., Yli-Juuti, T., and Virtanen, A.: Effect of Decreased Temperature on the Evaporation of α-Pinene Secondary Organic Aerosol Particles, ACS Earth Sp. Chem., 3, 2775–2785, https://doi.org/10.1021/acsearthspacechem.9b00240, 2019.

Liu, H. J., Zhao, C. S., Nekat, B., Ma, N., Wiedensohler, A., Van Pinxteren, D., Spindler, G., Müller, K., and Herrmann, H.: Aerosol hygroscopicity derived from

961 size-segregated chemical composition and its parameterization in the North China
962 Plain, Atmos. Chem. Phys., 14, 2525–2539, https://doi.org/10.5194/acp-14-2525-2014,
963 2014.

964 Liu, P. F., Zhao, C. S., Göbel, T., Hallbauer, E., Nowak, A., Ran, L., Xu, W. Y., Deng,
965 Z. Z., Ma, N., Mildenberger, K., Henning, S., Stratmann, F., and Wiedensohler, A.:
966 Hygroscopic properties of aerosol particles at high relative humidity and their diurnal
967 variations in the north China plain, Atmos. Chem. Phys., 11, 3479–3494,
968 https://doi.org/10.5194/acp-11-3479-2011, 2011.

969 Lu, Y., Yan, C., Fu, Y., Chen, Y., Liu, Y., Yang, G., Wang, Y., Bianchi, F., Chu, B.,
970 Zhou, Y., Yin, R., Baalbaki, R., Garmash, O., Deng, C., Wang, W., Liu, Y., Petäjä, T.,
971 Kerminen, V. M., Jiang, J., Kulmala, M., and Wang, L.: A proxy for atmospheric
972 daytime gaseous sulfuric acid concentration in urban Beijing, Atmos. Chem. Phys., 19,
973 1971–1983, https://doi.org/10.5194/acp-19-1971-2019, 2019.

974 Luoma, K., Virkkula, A., Aalto, P., Petäjä, T., and Kulmala, M.: Over a 10-year record
975 of aerosol optical properties at SMEAR II, Atmos. Chem. Phys., 19, 11363–11382,
976 https://doi.org/10.5194/acp-19-11363-2019, 2019.

977 Ma, C. Sen, Ma, G., and Pincebourde, S.: Survive a Warming Climate: Insect
978 Responses to Extreme High Temperatures, Annu. Rev. Entomol., 66, 163–184,
979 https://doi.org/10.1146/annurev-ento-041520-074454, 2021.

980 Ma, N., Zhao, C., Tao, J., Wu, Z., Kecorius, S., Wang, Z., Groß, J., Liu, H., Bian, Y.,
981 Kuang, Y., Teich, M., Spindler, G., Muller, K., Van Pinxteren, D., Herrmann, H., Hu,
982 M., and Wiedensohler, A.: Variation of CCN activity during new particle formation
983 events in the North China Plain, Atmos. Chem. Phys., 16, 8593–8607,
984 https://doi.org/10.5194/acp-16-8593-2016, 2016.

985 Marshall, S. F., Covert, D. S., and Charlson, R. J.: Relationship between asymmetry
986 parameter and hemispheric backscatter ratio: implications for climate forcing by
987 aerosols, Appl. Opt., 34, 5–6, 1995.

988 Merikanto, J., Spracklen, D. V, Mann, G. W., Pickering, S. J., and Carslaw, K. S.:
989 Atmospheric Chemistry and Physics Impact of nucleation on global CCN, Atmos.
990 Chem. Phys, 9, 8601–8616, 2009.

991 Mishchenko, M. I.: Electromagnetic scattering by nonspherical particles: A tutorial
992 review, J. Quant. Spectrosc. Radiat. Transf., 110, 808–832,
993 https://doi.org/10.1016/j.jqsrt.2008.12.005, 2009.

994 Moise, T., Flores, J. M., and Rudich, Y.: Optical Properties of Secondary Organic
995 Aerosols and Their Changes by Chemical Processes, Chem. Rev., 115, 4400–4439,
996 https://doi.org/10.1021/cr5005259, 2015.

997 Nairn, J. R. and Fawcett, R. J. B.: The excess heat factor: A metric for heatwave
998 intensity and its use in classifying heatwave severity, Int. J. Environ. Res. Public
999 Health, 12, 227–253, https://doi.org/10.3390/ijerph120100227, 2014.

1000 Petters, M. D. and Kreidenweis, S. M.: A single parameter representation of
1001 hygroscopic growth and cloud condensation nucleus activity, Atmos. Chem. Phys., 7,
1002 1961–1971, https://doi.org/10.5194/acp-7-1961-2007, 2007.

1003 Pierce, T. E. and Waldruff, P. S.: Pc-beis: A personal computer version of the biogenic
1004 emissions inventory system, J. Air Waste Manag. Assoc., 41, 937–941,
1005 https://doi.org/10.1080/10473289.1991.10466890, 1991.

1006 Qi, X. M., Ding, A. J., Nie, W., Petäjä, T., Kerminen, V. M., Herrmann, E., Xie, Y. N.,
1007 Zheng, L. F., Manninen, H., Aalto, P., Sun, J. N., Xu, Z. N., Chi, X. G., Huang, X.,
1008 Boy, M., Virkkula, A., Yang, X. Q., Fu, C. B., and Kulmala, M.: Aerosol size
1009 distribution and new particle formation in the western Yangtze River Delta of China:

2 years of measurements at the SORPES station, Atmos. Chem. Phys., 15, 12445–12464, https://doi.org/10.5194/acp-15-12445-2015, 2015.

Quinn, P. K., Bates, T. S., Baynard, T., Clarke, A. D., Onasch, T. B., Wang, W., Rood, M. J., Andrews, E., Allan, J., Carrico, C. M., Coffman, D., and Worsnop, D.: Impact of particulate organic matter on the relative humidity dependence of light scattering: A simplified parameterization, Geophys. Res. Lett., 32, 1–4, https://doi.org/10.1029/2005GL024322, 2005.

Ren, J., Chen, L., Fan, T., Liu, J., Jiang, S., and Zhang, F.: The NPF Effect on CCN Number Concentrations: A Review and Re-Evaluation of Observations From 35 Sites Worldwide, Geophys. Res. Lett., 48, 1–12, https://doi.org/10.1029/2021GL095190, 2021.

Rosati, B., Isokääntä, S., Christiansen, S., Jensen, M. M., Moosakutty, S. P., De Jonge, R. W., Massling, A., Glasius, M., Elm, J., Virtanen, A., and Bilde, M.: Hygroscopicity and CCN potential of DMS-derived aerosol particles, Atmos. Chem. Phys., 22, 13449–13466, https://doi.org/10.5194/acp-22-13449-2022, 2022.

Salma, I., Thén, W., Aalto, P., Kerminen, V. M., Kern, A., Barcza, Z., Petäjä, T., and Kulmala, M.: Influence of vegetation on occurrence and time distributions of regional new aerosol particle formation and growth, Atmos. Chem. Phys., 21, 2861–2880, https://doi.org/10.5194/acp-21-2861-2021, 2021.

Schuster, G. L., Dubovik, O., and Holben, B. N.: Angstrom exponent and bimodal aerosol size distributions, J. Geophys. Res. Atmos., 111, 1–14, https://doi.org/10.1029/2005JD006328, 2006.

Shang, D., Hu, M., Tang, L., Fang, X., Liu, Y., Wu, Y., Du, Z., Cai, X., Wu, Z., Lou, S., Hallquist, M., Guo, S., and Zhang, Y.: Significant effects of transport on nanoparticles during new particle formation events in the atmosphere of Beijing, Particuology, 80, 1–10, https://doi.org/10.1016/j.partic.2022.12.006, 2023.

1036 Sharma, S. and Mujumdar, P.: Increasing frequency and spatial extent of concurrent
1037 meteorological droughts and heatwaves in India, Sci. Rep., 7, 1–9,
1038 https://doi.org/10.1038/s41598-017-15896-3, 2017.

1039 Shen, X. J., Sun, J. Y., Zhang, Y. M., Wehner, B., Nowak, A., Tuch, T., Zhang, X. C.,
1040 Wang, T. T., Zhou, H. G., Zhang, X. L., Dong, F., Birmili, W., and Wiedensohler, A.:
1041 First long-term study of particle number size distributions and new particle formation
1042 events of regional aerosol in the North China Plain, Atmos. Chem. Phys., 11,
1043 1565–1580, https://doi.org/10.5194/acp-11-1565-2011, 2011.

1044 Su, Y. W.: The effects of extreme high temperature day off on electricity conservation,
1045 Weather. Clim. Soc., 13, 769–782, https://doi.org/10.1175/WCAS-D-20-0176.1, 2021.

1046 Sun, J., Hermann, M., Weinhold, K., Merkel, M., Birmili, W., Yang, Y., Flentje, H.,
1047 Ries, L., Couret, C., Elsasser, M., Sohmer, R., Wirtz, K., Meinhardt, F., Schü, M.,
1048 Bath, O., Hellack, B., Kerminen, V., Kulmala, M., Ma, N., and Wiedensohler, A.:
1049 Measurement report : Contribution of atmospheric new particle formation to ultrafine
1050 particle concentration , cloud condensation nuclei and radiative forcing : Results from
1051 five-year observations in Central Europe, Atmos. Chem. Phys., 1–34,
1052 https://doi.org/10.5194/acp-24-10667-2024, 2024.

1053 Sun, X., Sun, Q., Zhou, X., Li, X., Yang, M., Yu, A., and Geng, F.: Heat wave impact
1054 on mortality in Pudong New Area, China in 2013, Sci. Total Environ., 493, 789–794,
1055 https://doi.org/10.1016/j.scitotenv.2014.06.042, 2014.

1056 Sun, Y., Song, L., Yin, H., Zhang, X., Stott, P., Zhou, B., and Hu, T.: 20. Human
1057 influence on the 2015 extreme high temperature events in Western China, Bull. Am.
1058 Meteorol. Soc., 97, S102–S106, https://doi.org/10.1175/BAMS-D-16-0158.1, 2016.

1059 Tan, J., Zheng, Y., Song, G., Kalkstein, L. S., Kalkstein, A. J., and Tang, X.: Heat
1060 wave impacts on mortality in Shanghai, 1998 and 2003, Int. J. Biometeorol., 51,
1061 193–200, https://doi.org/10.1007/s00484-006-0058-3, 2007.

Tan, W., Yu, Y., Li, C., Li, J., Kang, L., Dong, H., Zeng, L., and Zhu, T.: Profiling Aerosol Liquid Water Content Using a Polarization Lidar, Environ. Sci. Technol., 54, 3129–3137, https://doi.org/10.1021/acs.est.9b07502, 2020.

Tang, M., Chan, C. K., Li, Y. J., Su, H., Ma, Q., Wu, Z., Zhang, G., Wang, Z., Ge, M., Hu, M., He, H., and Wang, X.: A review of experimental techniques for aerosol hygroscopicity studies, Atmos. Chem. Phys., 19, 12631–12686, https://doi.org/10.5194/acp-19-12631-2019, 2019.

Tao, L., Zhou, Z., Tao, J., Zhang, L., Wu, C., Li, J., Yue, D., Wu, Z., Zhang, Z., Yuan, Z., Huang, J., and Wang, B.: High contribution of new particle formation to ultrafine particles in four seasons in an urban atmosphere in south China, Sci. Total Environ., 889, https://doi.org/10.1016/j.scitotenv.2023.164202, 2023.

Teng, M., Liao, H., Burke, P. J., Chen, T., and Zhang, C.: Adaptive responses: the effects of temperature levels on residential electricity use in China, Clim. Change, 172, https://doi.org/10.1007/s10584-022-03374-3, 2022.

Tian, J., Wang, Q., Zhang, Y., Yan, M., Liu, H., Zhang, N., Ran, W., and Cao, J.: Impacts of primary emissions and secondary aerosol formation on air pollution in an urban area of China during the COVID-19 lockdown, Environ. Int., 150, 106426, https://doi.org/10.1016/j.envint.2021.106426, 2021.

Titos, G., Burgos, M. A., Zieger, P., Alados-Arboledas, L., Baltensperger, U., Jefferson, A., Sherman, J., Weingartner, E., Henzing, B., Luoma, K., O'Dowd, C., Wiedensohler, A., and Andrews, E.: A global study of hygroscopicity-driven light-scattering enhancement in the context of other in situ aerosol optical properties, Atmos. Chem. Phys., 21, 13031–13050, https://doi.org/10.5194/acp-21-13031-2021, 2021.

Titos, G., Cazorla, A., Zieger, P., Andrews, E., Lyamani, H., Granados-Muñoz, M. J., Olmo, F. J., and Alados-Arboledas, L.: Effect of hygroscopic growth on the aerosol

light-scattering coefficient: A review of measurements, techniques and error sources, Atmos. Environ., 141, 494–507, https://doi.org/10.1016/j.atmosenv.2016.07.021, 2016.

Titos, G., Jefferson, A., Sheridan, P. J., Andrews, E., Lyamani, H., Alados-Arboledas, L., and Ogren, J. A.: Aerosol light-scattering enhancement due to water uptake during the TCAP campaign, Atmos. Chem. Phys., 14, 7031–7043, https://doi.org/10.5194/acp-14-7031-2014, 2014.

Tritscher, T., Jurnyi, Z., Martin, M., Chirico, R., Gysel, M., Heringa, M. F., Decarlo, P. F., Sierau, B., Prévt, A. S. H., Weingartner, E., and Baltensperger, U.: Changes of hygroscopicity and morphology during ageing of diesel soot, Environ. Res. Lett., 6, https://doi.org/10.1088/1748-9326/6/3/034026, 2011.

Wang, N., Du, Y., Chen, D., Meng, H., Chen, X., Zhou, L., Shi, G., Zhan, Y., Feng, M., Li, W., Chen, M., Li, Z., and Yang, F.: Spatial disparities of ozone pollution in the Sichuan Basin spurred by extreme, hot weather, Atmos. Chem. Phys., 24, 3029–3042, https://doi.org/10.5194/acp-24-3029-2024, 2024.

Wang, Y., Li, Z., Zhang, R., Jin, X., Xu, W., Fan, X., Wu, H., Zhang, F., Sun, Y., Wang, Q., Cribb, M., and Hu, D.: Distinct Ultrafine- and Accumulation-Mode Particle Properties in Clean and Polluted Urban Environments, Geophys. Res. Lett., 46, 10918–10925, https://doi.org/10.1029/2019GL084047, 2019.

Wang, Z. B., Hu, M., Sun, J. Y., Wu, Z. J., Yue, D. L., Shen, X. J., Zhang, Y. M., Pei, X. Y., Cheng, Y. F., and Wiedensohler, A.: Characteristics of regional new particle formation in urban and regional background environments in the North China Plain, Atmos. Chem. Phys., 13, 12495–12506, https://doi.org/10.5194/acp-13-12495-2013, 2013.

Wang, Z., Wu, Z., Yue, D., Shang, D., Guo, S., Sun, J., Ding, A., Wang, L., Jiang, J., Guo, H., Gao, J., Cheung, H. C., Morawska, L., Keywood, M., and Hu, M.: New

particle formation in China: Current knowledge and further directions, Sci. Total Environ., 577, 258–266, https://doi.org/10.1016/j.scitotenv.2016.10.177, 2017.

Westervelt, D. M., Pierce, J. R., Riipinen, I., Trivitayanurak, W., Hamed, A., Kulmala, M., Laaksonen, A., Decesari, S., and Adams, P. J.: Formation and growth of nucleated particles into cloud condensation nuclei: Model-measurement comparison, Atmos. Chem. Phys., 13, 7645–7663, https://doi.org/10.5194/acp-13-7645-2013, 2013.

Wu, Z. J., Poulain, L., Birmili, W., Größ, J., Niedermeier, N., Wang, Z. B., Herrmann, H., and Wiedensohler, A.: Some insights into the condensing vapors driving new particle growth to CCN sizes on the basis of hygroscopicity measurements, Atmos. Chem. Phys., 15, 13071–13083, https://doi.org/10.5194/acp-15-13071-2015, 2015.

Wu, Z. J., Zheng, J., Shang, D. J., Du, Z. F., Wu, Y. S., Zeng, L. M., Wiedensohler, A., and Hu, M.: Particle hygroscopicity and its link to chemical composition in the urban atmosphere of Beijing, China, during summertime, Atmos. Chem. Phys., 16, 1123–1138, https://doi.org/10.5194/acp-16-1123-2016, 2016.

Xia, C., Sun, J., Hu, X., Shen, X., Zhang, Y., Zhang, S., Wang, J., Liu, Q., Lu, J., Liu, S., and Zhang, X.: Effects of hygroscopicity on aerosol optical properties and direct radiative forcing in Beijing: Based on two-year observations, Sci. Total Environ., 857, 159233, https://doi.org/10.1016/j.scitotenv.2022.159233, 2023.

Xu, W. Y., Zhao, C. S., Ran, L., Deng, Z. Z., Liu, P. F., Ma, N., Lin, W. L., Xu, X. B., Yan, P., He, X., Yu, J., Liang, W. D., and Chen, L. L.: Characteristics of pollutants and their correlation to meteorological conditions at a suburban site in the North China Plain, Atmos. Chem. Phys., 11, 4353–4369, https://doi.org/10.5194/acp-11-4353-2011, 2011.

Xu, W., Chen, C., Qiu, Y., Xie, C., Chen, Y., Ma, N., Xu, W., Fu, P., Wang, Z., Pan, X., Zhu, J., Ngcg, N. L., and Sun, Y.: Size-resolved characterization of organic

aerosol in the North China Plain: New insights from high resolution spectral analysis, Environ. Sci. Atmos., 1, 346–358, https://doi.org/10.1039/d1ea00025j, 2021.

Xu, W., Kuang, Y., Xu, W., Zhang, Z., Luo, B., Zhang, X., Tao, J., Qiao, H., Liu, L., and Sun, Y.: Hygroscopic growth and activation changed submicron aerosol composition and properties in the North China Plain, Atmos. Chem. Phys., 24, 9387–9399, https://doi.org/10.5194/acp-24-9387-2024, 2024.

Xue, B., Kuang, Y., Xu, W., and Zhao, P.: Joint increase of aerosol scattering efficiency and aerosol hygroscopicity aggravate visibility impairment in the North China Plain, Sci. Total Environ., 839, 141163, https://doi.org/10.1016/j.scitotenv.2022.156279, 2022.

Yang, P., Feng, Q., Hong, G., Kattawar, G. W., Wiscombe, W. J., Mishchenko, M. I., Dubovik, O., Laszlo, I., and Sokolik, I. N.: Modeling of the scattering and radiative properties of nonspherical dust-like aerosols, J. Aerosol Sci., 38, 995–1014, https://doi.org/10.1016/j.jaerosci.2007.07.001, 2007.

Yarragunta, Y., Srivastava, S., Mitra, D., and Chandola, H. C.: Source apportionment of carbon monoxide over India: a quantitative analysis using MOZART-4, Environ. Sci. Pollut. Res., 28, 8722–8742, https://doi.org/10.1007/s11356-020-11099-y, 2021.

Yuan, L. and Zhao, C.: Quantifying particle-To-particle heterogeneity in aerosol hygroscopicity, Atmos. Chem. Phys., 23, 3195–3205, https://doi.org/10.5194/acp-23-3195-2023, 2023.

Zhang, L., Sun, J. Y., Shen, X. J., Zhang, Y. M., Che, H., Ma, Q. L., Zhang, Y. W., Zhang, X. Y., and Ogren, J. A.: Observations of relative humidity effects on aerosol light scattering in the Yangtze River Delta of China, Atmos. Chem. Phys., 15, 8439–8454, https://doi.org/10.5194/acp-15-8439-2015, 2015.

Zhang, R., Khalizov, A. F., Pagels, J., Zhang, D., Xue, H., and McMurry, P. H.: Variability in morphology, hygroscopicity, and optical properties of soot aerosols

during atmospheric processing, Proc. Natl. Acad. Sci. U. S. A., 105, 10291–10296, https://doi.org/10.1073/pnas.0804860105, 2008.

Zhang, R., Khalizov, A., Wang, L., Hu, M., and Xu, W.: Nucleation and growth of nanoparticles in the atmosphere, Chem. Rev., 112, 1957–2011, https://doi.org/10.1021/cr2001756, 2012.

Zhang, R., Suh, I., Zhao, J., Zhang, D., Fortner, E. C., Tie, X., Molina, L. T., and Molina, M. J.: Atmospheric new particle formation enhanced by organic acids, Science (80-.)., 304, 1487–1490, https://doi.org/10.1126/science.1095139, 2004.

Zhang, R., Wang, G., Guo, S., Zamora, M. L., Ying, Q., Lin, Y., Wang, W., Hu, M., and Wang, Y.: Formation of Urban Fine Particulate Matter, Chem. Rev., 115, 3803–3855, https://doi.org/10.1021/acs.chemrev.5b00067, 2015.

Zhang, Z., Xu, W., Zeng, S., Liu, Y., Liu, T., Zhang, Y., Du, A., Li, Y., Zhang, N., Wang, J., Aruffo, E., Han, P., Li, J., Wang, Z., and Sun, Y.: Secondary Organic Aerosol Formation from Ambient Air in Summer in Urban Beijing: Contribution of S/IVOCs and Impacts of Heat Waves, Environ. Sci. Technol. Lett., https://doi.org/10.1021/acs.estlett.4c00415, 2024.

Zhao, C., Yu, Y., Kuang, Y., Tao, J., and Zhao, G.: Recent Progress of Aerosol Light-scattering Enhancement Factor Studies in China, Adv. Atmos. Sci., 36, 1015–1026, https://doi.org/10.1007/s00376-019-8248-1, 2019.

Zhao, G., Hu, M., Fang, X., Tan, T., Xiao, Y., Du, Z., Zheng, J., Shang, D., Wu, Z., Guo, S., and Zhao, C.: Larger than expected variation range in the real part of the refractive index for ambient aerosols in China, Sci. Total Environ., 779, 146443, https://doi.org/10.1016/j.scitotenv.2021.146443, 2021.

Zhao, S., Yu, Y., Li, J., Yin, D., Qi, S., and Qin, D.: Response of particle number concentrations to the clean air action plan: Lessons from the first long-term aerosol

measurements in a typical urban valley in western China, Atmos. Chem. Phys., 21, 14959–14981, https://doi.org/10.5194/acp-21-14959-2021, 2021.

Zhu, Y., Shen, Y., Li, K., Meng, H., Sun, Y., Yao, X., Gao, H., Xue, L., and Wang, W.: Investigation of Particle Number Concentrations and New Particle Formation With Largely Reduced Air Pollutant Emissions at a Coastal Semi-Urban Site in Northern China, J. Geophys. Res. Atmos., 126, 1–20, https://doi.org/10.1029/2021JD035419, 2021.

Zieger, P., Weingartner, E., Henzing, J., Moerman, M., De Leeuw, G., Mikkilä, J., Ehn, M., Petäjä, T., Clémer, K., Van Roozendael, M., Yilmaz, S., Frieß, U., Irie, H., Wagner, T., Shaiganfar, R., Beirle, S., Apituley, A., Wilson, K., and Baltensperger, U.: Comparison of ambient aerosol extinction coefficients obtained from in-situ, MAX-DOAS and LIDAR measurements at Cabauw, Atmos. Chem. Phys., 11, 2603–2624, https://doi.org/10.5194/acp-11-2603-2011, 2011.